Chapter VII

CHAPTER VII

DIVALENT METAL (II) COMPLEXES OF 1-NAPHTHOIC ACID, WITH AMINOGUANIDINE: SYNTHESIS, CHARACTERIZATION, AND ITS APPLICATION IN HYDROGEN EVOLUTION REACTION AND CORROSION INHIBITION STUDIES

7.1 INTRODUCTION

Aminoguanidine is a hydrazine derivative and is composed of a carbon atom and four nitrogen atoms that are coordinated at various positions to form a mono (+1) or di (+2) cation the hybridization mode is also distinct, with the hydrazine moiety exhibiting sp3 hybridization and the non-hydrogen atoms showing sp2 hybridization. 1-naphthoic acid has an outstanding ability to coordinate with metal ions, which leads to stable complex formation [1]. So far, no investigation has been carried out with the 1-naphthoic acid with aminoguanidine and transition alkali metal & alkaline earth metal ions. Systematic synthesis and characterization by analytical, spectral, thermal, and structural methods of complexes were carried out. Antibacterial activity towards *Escherichia coli* and *Staphylococcus aureus* was also studied. Further complexes show good cytotoxic effects towards MCF-7(breast cancer) and A-549 (lung cancer). The proposed research also examines the electrocatalytic activity of alkaline and alkali earth metals for hydrogen evolution reaction in an acid solution. In addition to that nano metal oxides are synthesized from corresponding complexes and characterized systematically and show an anticorrosive property in acidic solutions, namely, HCl, H_2SO_4, and H_3PO_4. The corrosion study of mild steel was done with electrochemical techniques.

7.2 EXPERIMENTAL PROCEDURE

7.2.1. Preparation method

0.36 g of aminoguanidine bicarbonate was stirred at room temperature with 0.17g of 1-naphthoic acid to form a clear aqueous solution. To the obtained solution, metal ions were added, and the overall ratio was (1:2:2). The resulting solution was set aside in a water

bath to reduce the volume of the solution and then kept at room temperature to obtain microcrystal. The microcrystal was filtered using filter paper, dried, and washed with ethanol. The schematic illustration is shown in **Figure 7.1** [2].

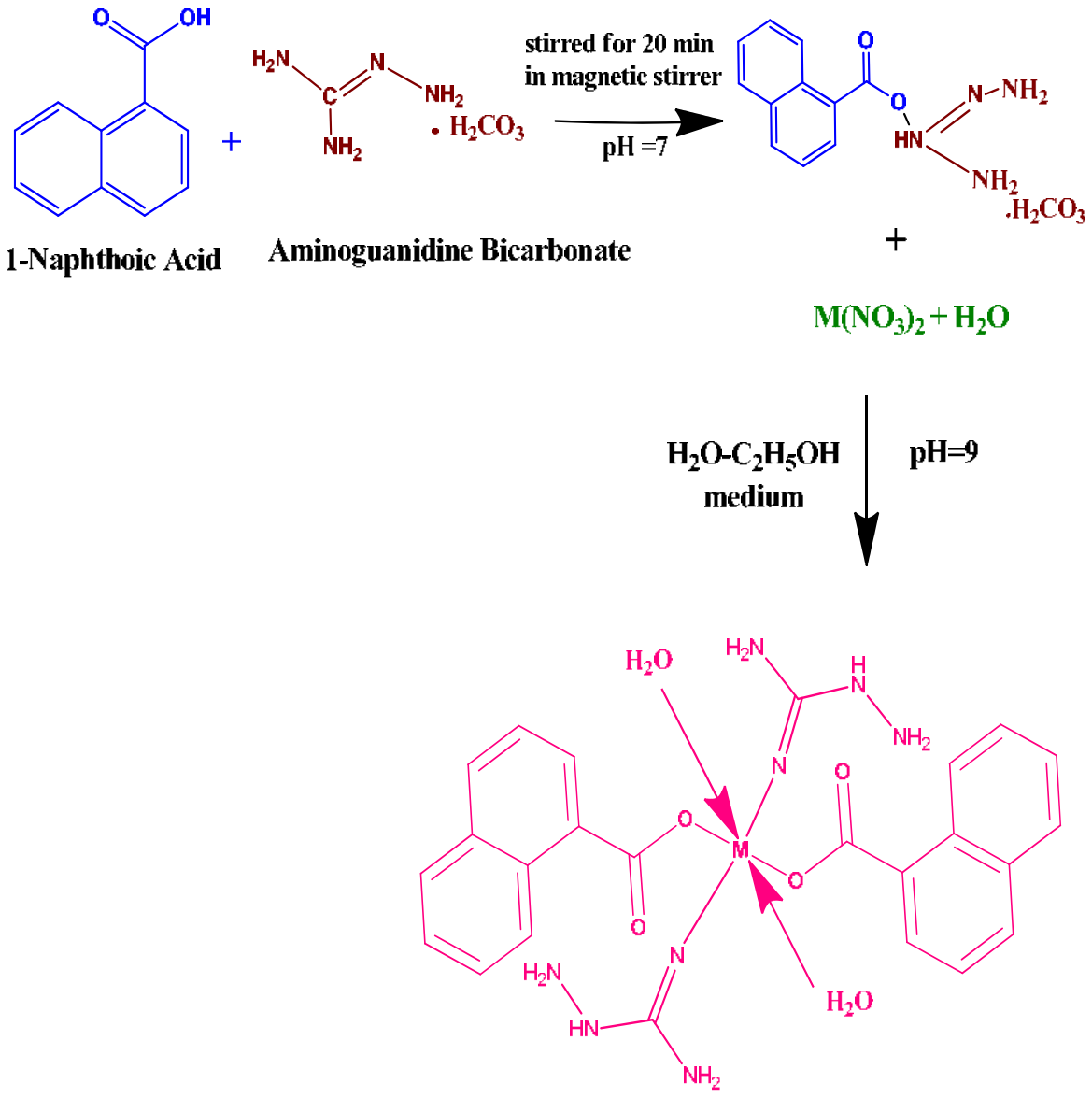

Figure 7.1 *Pathway for the synthesis of a compound*

7.3 RESULTS AND DISCUSSION

7.3.1 Analytical Data

The expected values agreed well with the elemental data analysis, which shows the formation of metal complexes as shown in **Tables 7.1** and **7.2**.

7.3.2 FT-IR analysis

Figure 7.2 (a-m) and **Table 7.3** depict the spectral band of metal complexes. Symmetric and asymmetric stretching frequencies of the carboxylate ions are assigned in the regions of 1359-1438 cm^{-1} and 1531-1704 cm^{-1}. N-N stretching of aminoguanidine is shown at 1108-11061 cm^{-1}. When complex FT-IR is compared with ligand, which was discussed in chapter-IV, the complexes have large peaks of about 3241-3498 cm^{-1} which suggests O-H frequencies. N-H stretching frequency was found at 3200 cm^{-1}. The existence of aminoguanidine in the complex was demonstrated by N-N frequencies, which were found in a range of 1046-1108 cm^{-1}. The peak is around 680-776 cm^{-1} due to M-O vibration.

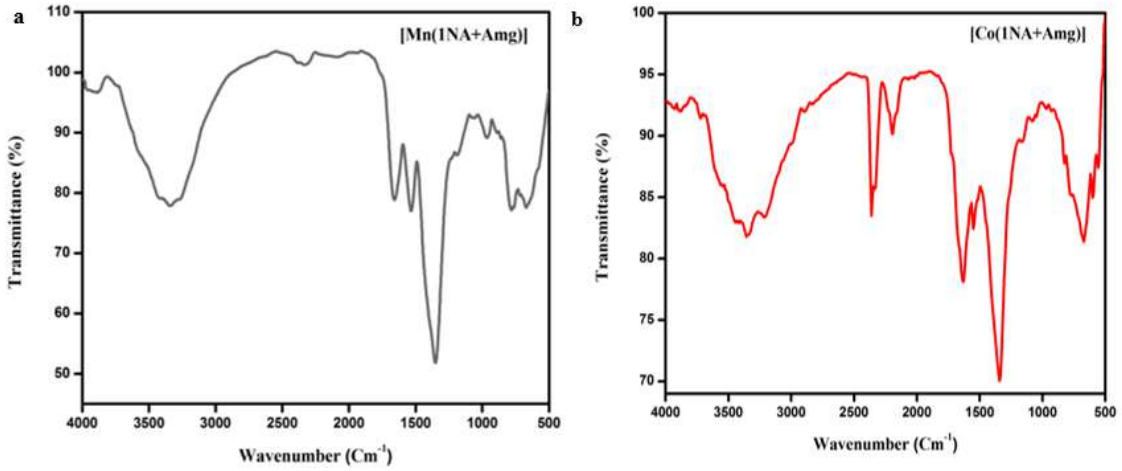

Figure 7.2 *FT-IR spectra of a)Mn(II) b)Co(II) complex*

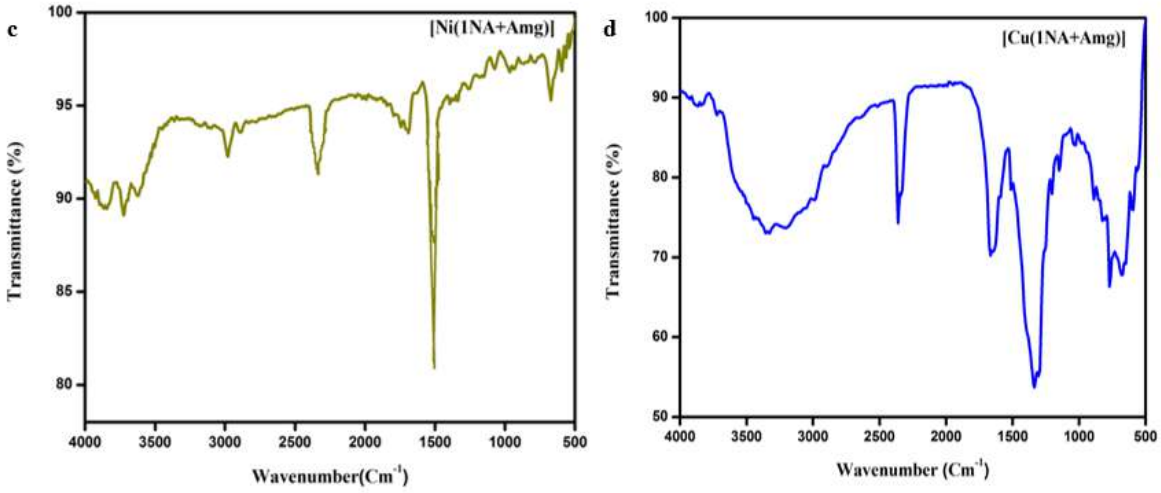

Figure 7.2 *FT-IR spectra of c)Ni(II) d)Cu(II) complex*

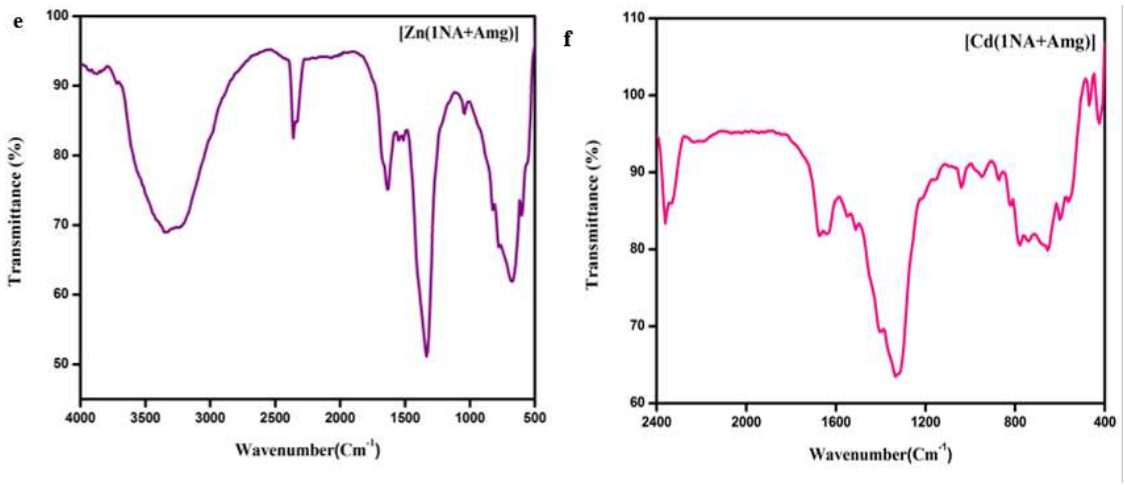

Figure 7.2 *FT-IR spectra of e) Zn (II) f)Cd(II) complex*

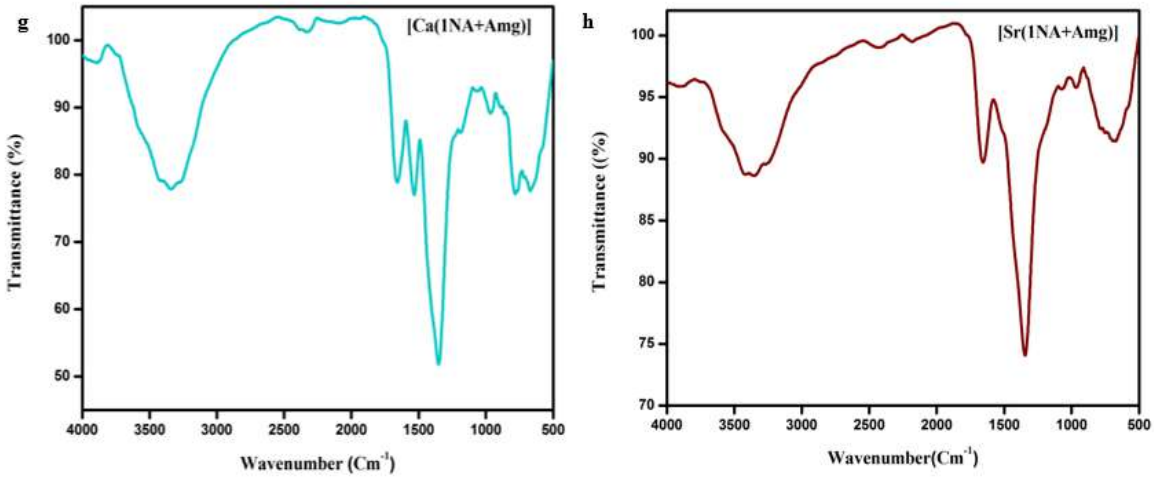

Figure 7.2 *FT-IR spectra of g)Ca(II) h)Sr(II) complex*

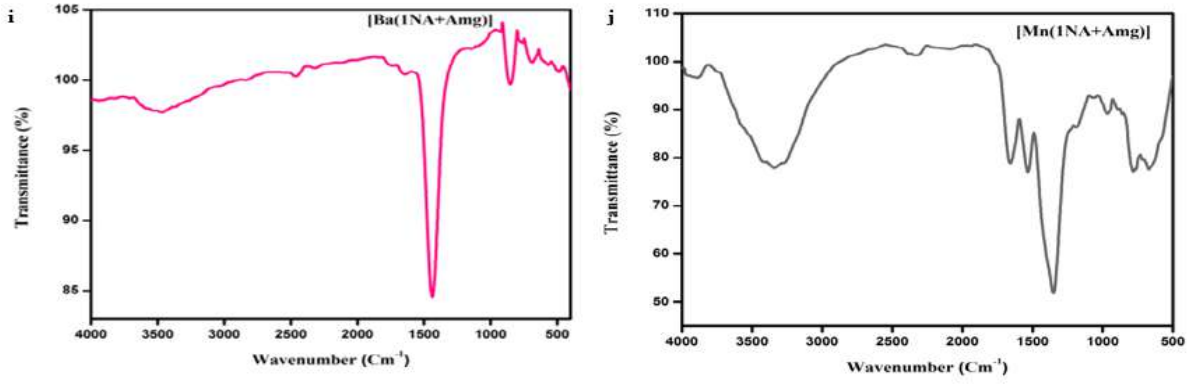

Figure 7.2 *FT-IR spectra of i) Ba (II) j)Mn (II) complex*

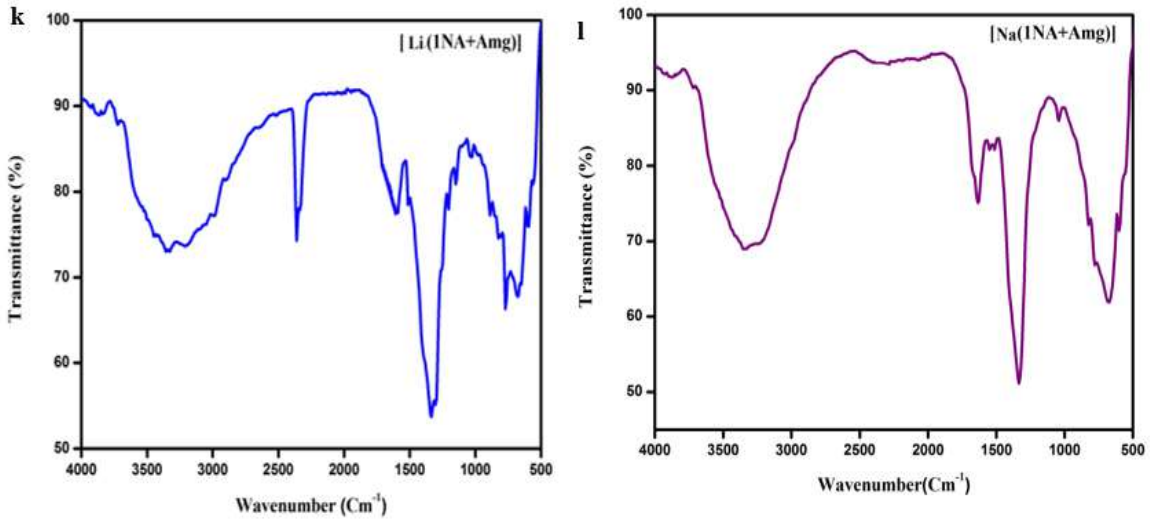

Figure 7.2 *FT-IR spectra of k) Li (I) l) Na (I) complex*

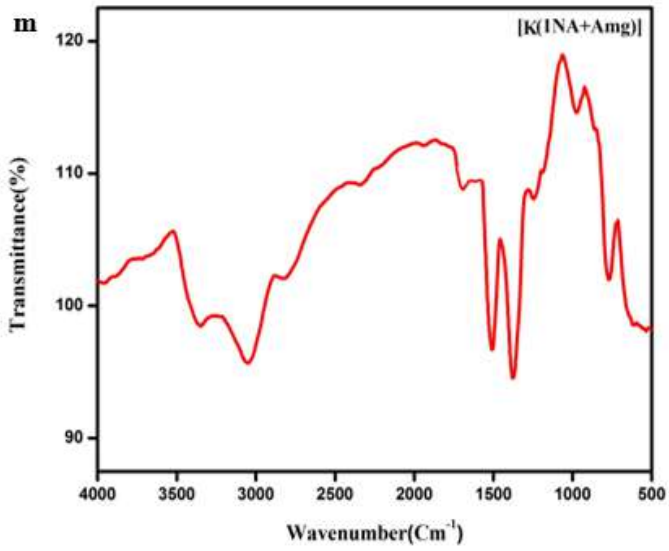

Figure 7.2 *FT-IR spectra of m) K(I) complex*

Table 7.1 *Analytical data*								
Metal Complexes	**Molecular weight (g/mol)**	**Color**	**pH**	**Melting point (°C)**	**Metal (%)**		**Hydrazine (%)**	
					Found	**Calc**	**Found**	**Calc**
[Mn($C_2H_8N_4O_3$)$_2$ {$C_{10}H_7$(1-COO)}$_2$.2H $_2$O]	594.46	Light pink	7	223	9.4	9.5	15.1	16.3
[Co ($C_2H_8N_4O_3$)$_2$ {$C_{10}H_7$(1-COO)}$_2$.2H $_2$O]	598.45	Pink	6	158	9.8	10.6	15.5	15.2
[Ni ($C_2H_8N_4O_3$)$_2$ {$C_{10}H_7$(1-COO)}$_2$.2H $_2$O]	598.21	Green	7	163	18.7	17.9	14.9	14.5
[Cu ($C_2H_8N_4O_3$)$_2$ {$C_{10}H_7$(1-COO)}$_2$.2H $_2$O]	603.07	Blue	8	186	10.54	9.6	16.5	16.5
[Zn ($C_2H_8N_4O_3$)$_2$ {$C_{10}H_7$(1-COO)}$_2$.2H $_2$O]	604.90	Duty white	8	192	10.81	10.6	15.7	15.3
[Cd ($C_2H_8N_4O_3$)$_2$ {$C_{10}H_7$(1-COO)}$_2$.2H $_2$O]	651.93	white	7	203	17.24	16.9	14.8	14.5
[Ca ($C_2H_8N_4O_3$)$_2$ {$C_{10}H_7$(1-COO)}$_2$.2H $_2$O]	579.60	White	7	259	17.7	16.9	16.9	15.5
[Sr ($C_2H_8N_4O_3$)$_2$ {$C_{10}H_7$(1-COO)}$_2$.2H $_2$O]	627.14	White	6	239	13.97	12.87	18.5	17.5
[Ba ($C_2H_8N_4O_3$)$_2$ {$C_{10}H_7$(1-COO)}$_2$.2H $_2$O]	676.85	White	6	203	20.29	20.1	16.7	16.3
[Mg ($C_2H_8N_4O_3$)$_2$ {$C_{10}H_7$(1-COO)}$_2$.2H $_2$O]	563.83	White	6	244	18.24	18.9	17.8	17.5
[Li ($C_2H_8N_4O_3$)$_2$ {$C_{10}H_7$(1-COO)}$_2$.2H $_2$O]	335.28	white	6	237	11.31	11.3	17.5	17.5
[Na ($C_2H_8N_4O_3$)$_2$ {$C_{10}H_7$(1-COO)}$_2$.2H $_2$O]	351.33	white	6	212	14.20	14.19	16.7	16.4
[K ($C_2H_8N_4O_3$)$_2$ {$C_{10}H_7$(1-COO)}$_2$.2H $_2$O]	367.44	white	6	205	16.9	16.8	15.8	15.5

Table 7.2 *Elemental data*				
Complexes	**% Carbon Found (Cald)**	**% Hydrogen Found (Cald)**	**% Nitrogen Found (Cald)**	**% Oxygen Found (Cald)**
[Mn($C_2H_8N_4O_3$)$_2$ {C_{10}H7(1-COO)}$_2$.2H $_2$O]	48.49(48.47)	4.58(4.60)	18.85(18.77)	18.84(18.87)
[Co ($C_2H_8N_4O_3$)$_2$ {C_{10}H7(1-COO)}$_2$.2H $_2$O]	48.17(48.00)	4.55(4.40)	18.72(18.69)	18.71(18.70)
[Ni ($C_2H_8N_4O_3$)$_2$ {C_{10}H7(1-COO)}$_2$.2H $_2$O]	48.19(48.11)	4.56(4.52)	18.73(18.71)	18.72(18.11)
[Cu ($C_2H_8N_4O_3$)$_2$ {C_{10}H7(1-COO)}$_2$.2H $_2$O]	47.80(47.20)	4.51(4.20)	18.58(18.25)	18.57(18.50)
[Zn ($C_2H_8N_4O_3$)$_2$ {C_{10}H7(1-COO)}$_2$.2H $_2$O]	47.65(47.02)	4.50(4.20)	18.52(18.49)	18.51(18.44)
[Cd ($C_2H_8N_4O_3$)$_2$ {C_{10}H7(1-COO)}$_2$.2H $_2$O]	44.22(44.10)	4.17(4.01)	17.19(17.01)	17.18(17.11)
[Ca ($C_2H_8N_4O_3$)$_2$ {C_{10}H7(1-COO)}$_2$.2H $_2$O]	49.73(49.52)	4.704.69)	19.33(19.30)	19.32(19.30)
[Sr ($C_2H_8N_4O_3$)$_2$ {C_{10}H7(1-COO)}$_2$.2H $_2$O]	45.96(45.06)	4.34(4.30)	17.87(17.81)	17.86(17.79)
[Ba ($C_2H_8N_4O_3$)$_2$ {C_{10}H7(1-COO)}$_2$.2H $_2$O]	42.59(41.33)	4.02(4.00)	16.56(16.49)	16.55(16.50)
[Mg ($C_2H_8N_4O_3$)$_2$ {C_{10}H7(1-COO)}$_2$.2H $_2$O]	51.13(50.11)	4.83(4.80)	19.87(19.79)	19.86(19.80)
[Li ($C_2H_8N_4O_3$)$_2$ {C_{10}H7(1-COO)}$_2$.2H $_2$O]	58.1858.10)	4.88(4.00)	22.62(22.60)	12.90(12.89)
[Na ($C_2H_8N_4O_3$)$_2$ {C_{10}H7(1-COO)}$_2$.2H $_2$O]	48.31(48.30)	5.51(5.49)	27.04(27.01)	15.44(15.40)
[K ($C_2H_8N_4O_3$)$_2$ {C_{10}H7(1-COO)}$_2$.2H $_2$O]	47.09(47.01)	5.37(5.30)	26.36(26.30)	15.05(15.02)

Table 7.3 *IR Spectral data*						
Complexes	**$\nu_{(OH)}$ cm^{-1}**	**ν_{asym} (C=O) cm^{-1}**	**υ_{sym} (C=O) cm^{-1}**	**$\upsilon_{(NH)}$ cm^{-1}**	**$\upsilon_{(N-N)}$ cm^{-1}**	**M-O cm^{-1}**
[Mn($C_2H_8N_4O_3$)$_2$ {$C_{10}H7(1\text{-}COO)$}$_2$.2H $_2$O]	3035	1667	1530	3371	1097	498
[Co ($C_2H_8N_4O_3$)$_2$ {$C_{10}H7(1\text{-}COO)$}$_2$.2H $_2$O]	3175	1671	1541	3342	1086	499
[Ni ($C_2H_8N_4O_3$)$_2$ {$C_{10}H7(1\text{-}COO)$}$_2$.2H $_2$O]	3115	1669	1518	3658	1212	487
[Cu ($C_2H_8N_4O_3$)$_2$ {$C_{10}H7(1\text{-}COO)$}$_2$.2H $_2$O]	3047	162	152	3361	1087	497
[Zn ($C_2H_8N_4O_3$)$_2$ {$C_{10}H7(1\text{-}COO)$}$_2$.2H $_2$O]	3073	1668	1517	3321	1109	499
[Cd ($C_2H_8N_4O_3$)$_2$ {$C_{10}H7(1\text{-}COO)$}$_2$.2H $_2$O]	3035	1658	1515	3342	1110	488
[Ca ($C_2H_8N_4O_3$)$_2$ {$C_{10}H7(1\text{-}COO)$}$_2$.2H $_2$O]	3132	1647	1511	3353	1332	462
[Sr ($C_2H_8N_4O_3$)$_2$ {$C_{10}H7(1\text{-}COO)$}$_2$.2H $_2$O]	3192	1619	1558	3374	1382	491
[Ba ($C_2H_8N_4O_3$)$_2$ {$C_{10}H7(1\text{-}COO)$}$_2$.2H $_2$O]	3241	1639	1528	3423	1352	498
[Mg ($C_2H_8N_4O_3$)$_2$ {$C_{10}H7(1\text{-}COO)$}$_2$.2H $_2$O]	3320	1639	1481	3877	1019	485
[Li ($C_2H_8N_4O_3$)$_2$ {$C_{10}H7(1\text{-}COO)$}$_2$.2H $_2$O]	3325	1589	1350	3250	1139	440
[Na ($C_2H_8N_4O_3$)$_2$ {$C_{10}H7(1\text{-}COO)$}$_2$.2H $_2$O]	3309	1573	1342	3232	1108	470
[K ($C_2H_8N_4O_3$)$_2$ {$C_{10}H7(1\text{-}COO)$}$_2$.2H $_2$O]	3345	1581	1334	3260	1125	447

7.3.3 Electronic spectra

All the metal complexes were dissolved in DMSO, and they were determined in electronic spectra in a room environment which is exhibited in **Figure 7.3(a-m)**. The absorption band for Mn^{2+}, Co^{2+}, Ni^{2+}, Cu^{2+}, Zn^{2+}, Cd^{2+}, Mg^{2+}, Ca^{2+}, Sr^{2+}, Ba^{2+}, Li^{+}, Na^{+}, and K^{+} shows the π-π* transition of the ligand group, and some less intense peaks that exhibit around the 400-480 nm range exhibit the d-d transition of the metal peaks. For, Ni^{2+} ion the transistion occurred at $^{3}A2g(F) \rightarrow {}^{3}T1g$ (F) and $^{3}A2g(F) \rightarrow {}^{3}T1g$ (P), Co^{2+} represents $^{4}T1g$ (F) → $^{4}A2g(F)$ and $^{4}T1g$ (F) → $^{4}T2g$ (P), Cu^{2+} exhibits $^{2}B1g \rightarrow {}^{2}Fg$ and $^{2}E1g \rightarrow {}^{2}A1g$. The bands confirm the presence of a distorted octahedral configuration for the Cu (II) complex. The intensity of Mn(II) complexes is very weak compared to others due to spin-forbidden transitions. For Ca^{2+}, Sr^{2+}, and Ba^{2+}, it exhibits the $^{2}S_{1/2} \rightarrow {}^{2}P^{o}_{3/2}$ transistion [3].

The direct band gap energy for all the metal complexes was calculated from the below equation under optical conditions.

$$(\alpha\hbar\upsilon)^{n} = A(\hbar\upsilon - Eg) \qquad \textbf{Eq.(7.1)}$$

where E, is the energy gap, α is the optical absorption coefficient, h is Planck's constant, υ is the frequency of light, A is the constant, and n = 2 for direct band gap energy. The band gap was drawn by extrapolating the straight line of the graph ($\alpha\hbar\upsilon$) versus ($\hbar\upsilon$) on the energy axis **(Figure 7.3(a'-m'))**, the band gap energy was found to be 2.5-4.6 eV.

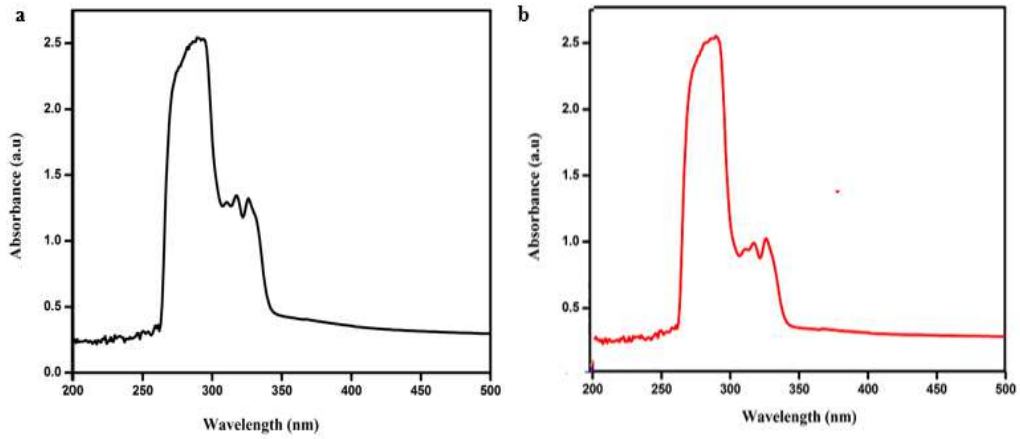

Figure 7.3 *UV-visible spectra of a) Mn (II) b) Co (II) complex*

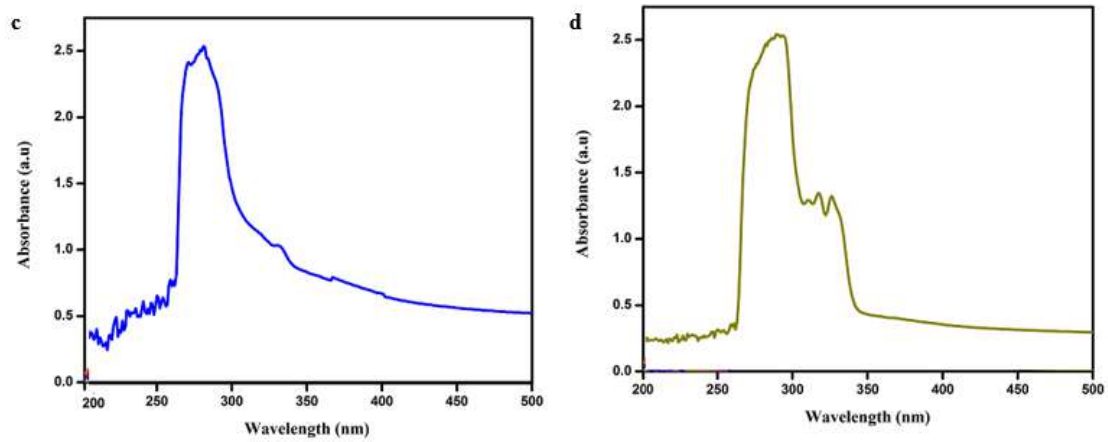

Figure 7.3 *UV-visible spectra of c) Ni (II) d) Cu (II) complex*

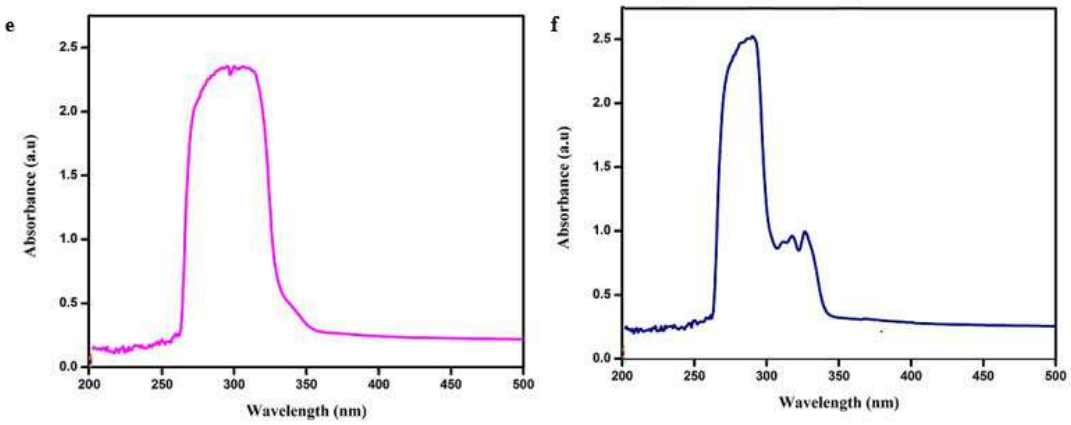

Figure 7.3 *UV-visible spectra of e) Zn (II) f) Cd (II) complex*

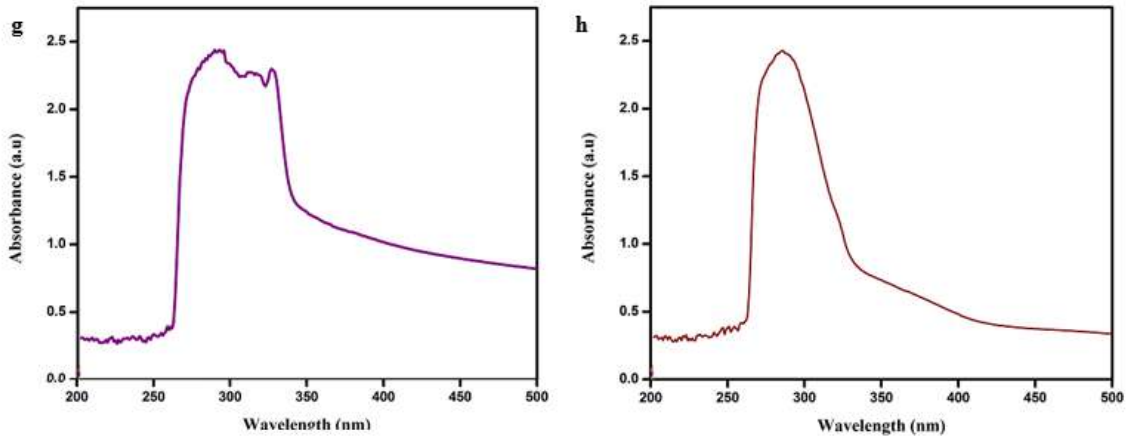

Figure 7.3 *UV-visible spectra of g) Ca (II) h) Sr (II) complex*

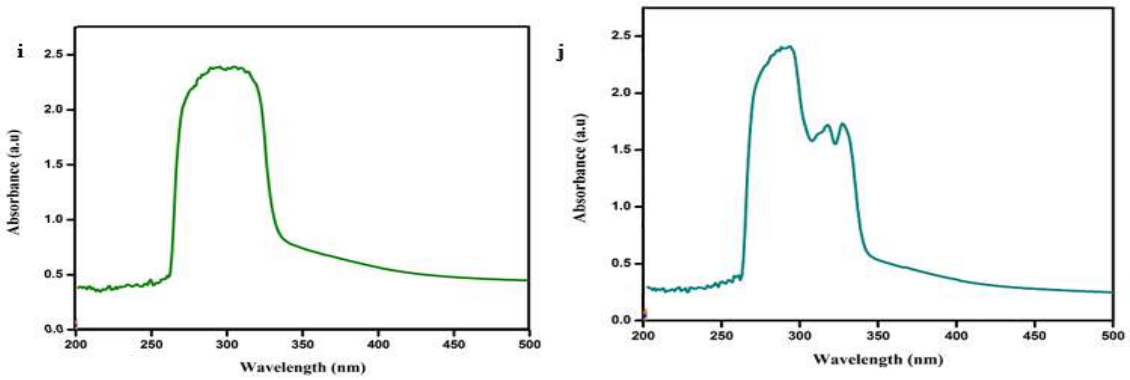

Figure 7.3 *UV-visible spectra of i) Ba (II) j) Mg (II) complex*

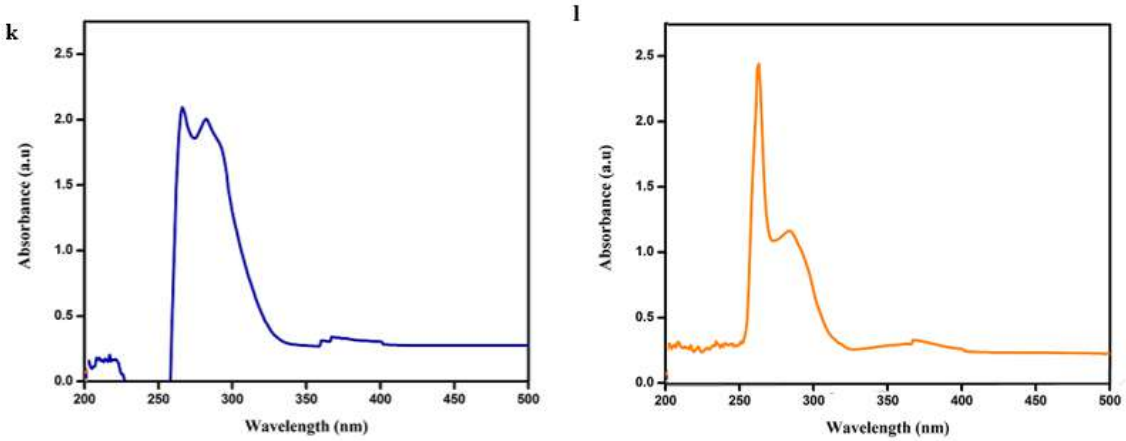

Figure 7.3 *UV-visible spectra of k) Li (I) l) Na (I) complex*

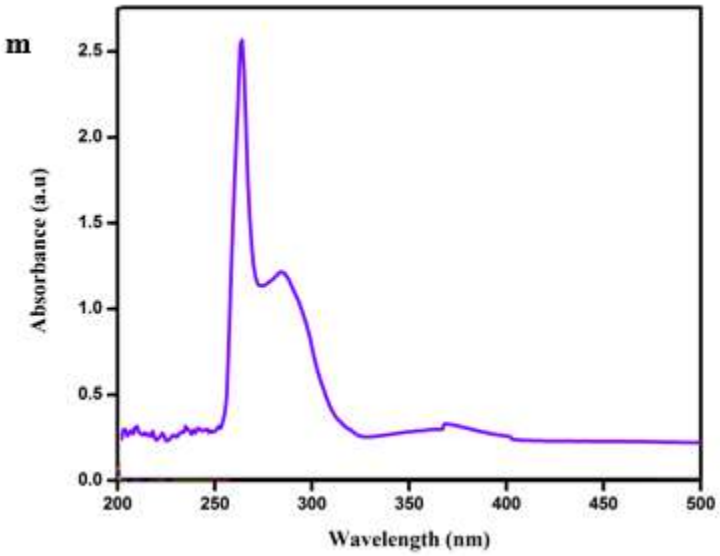

Figure 7.3 *UV-visible spectra of m) K (I) complex*

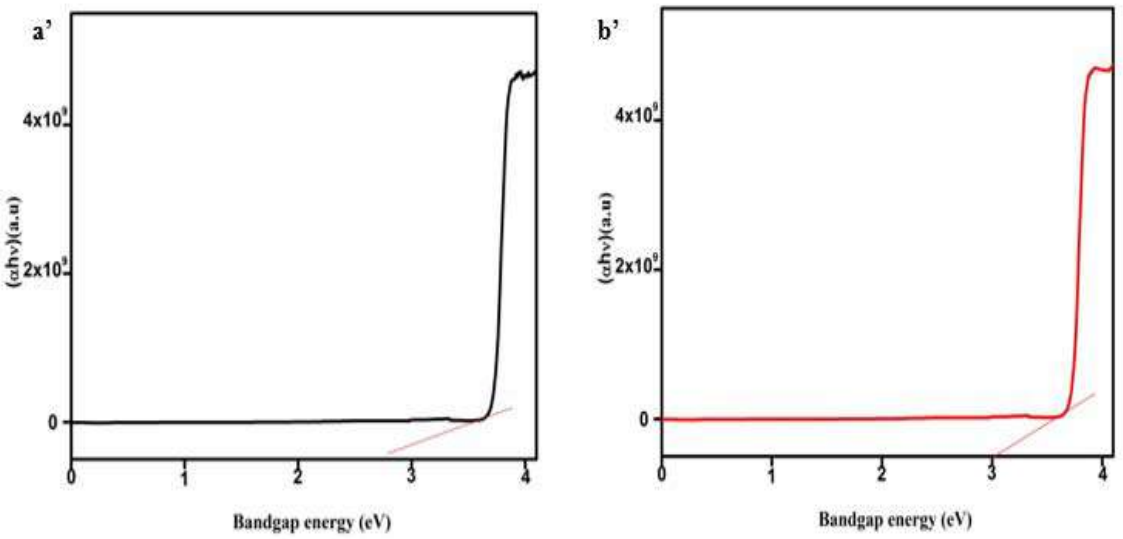

Figure 7.3 *UV-visible spectra of a') Mn (II) b') Co (II) complex*

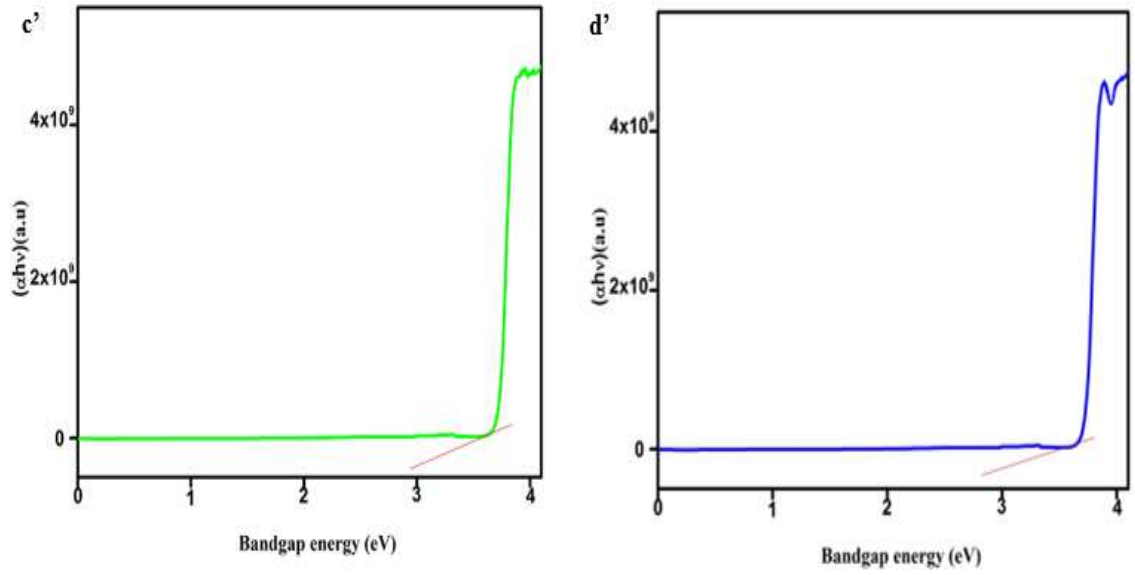

Figure 7.3 *UV-visible spectra of c') Ni (II) d') Cu (II) complex*

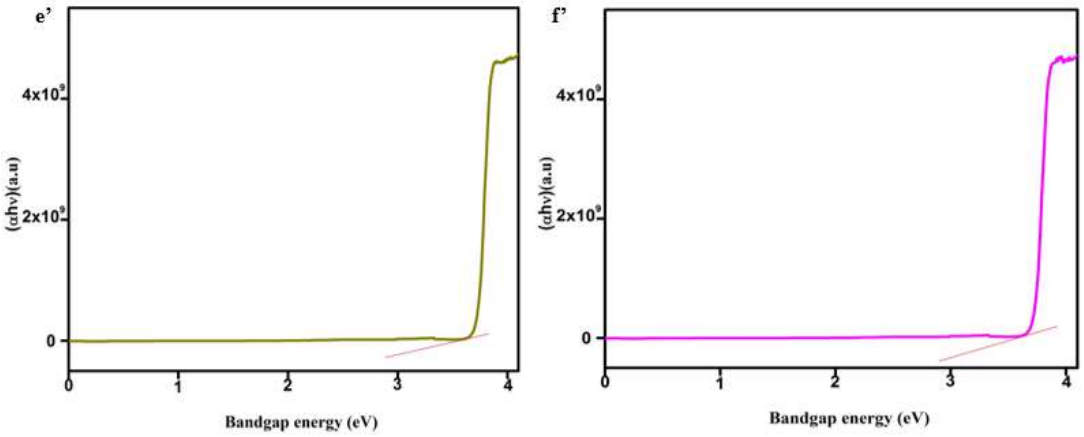

Figure 7.3 *UV-visible spectra of e') Zn (II) f') Cd (II) complex*

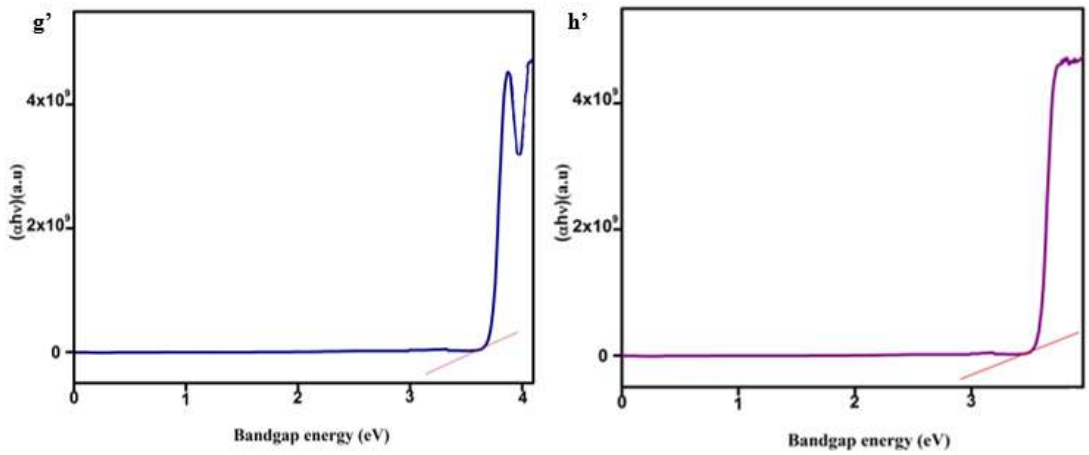

Figure 7.3 *UV-visible spectra of g') Ca (II) h') Sr (II) complex*

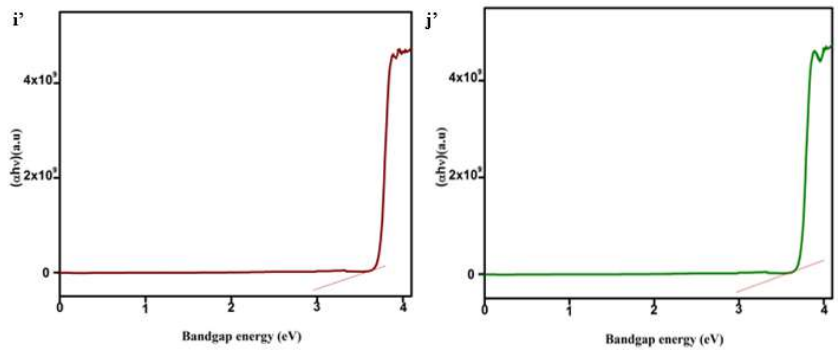

Figure 7.3 *UV-visible spectra of i') Ba (II) j') Mg (II) complex*

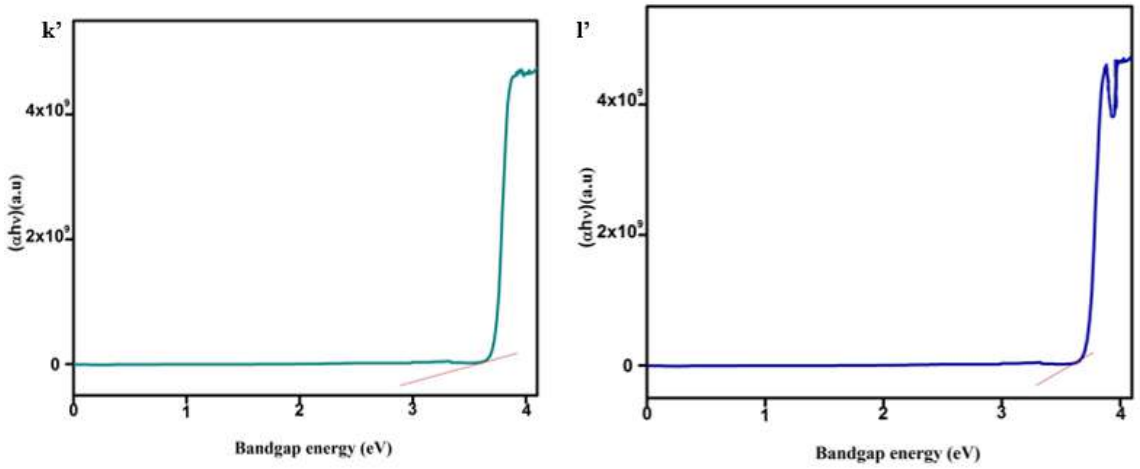

Figure 7.3 *UV-visible spectra of k') Li (I) l') Na (I) complex*

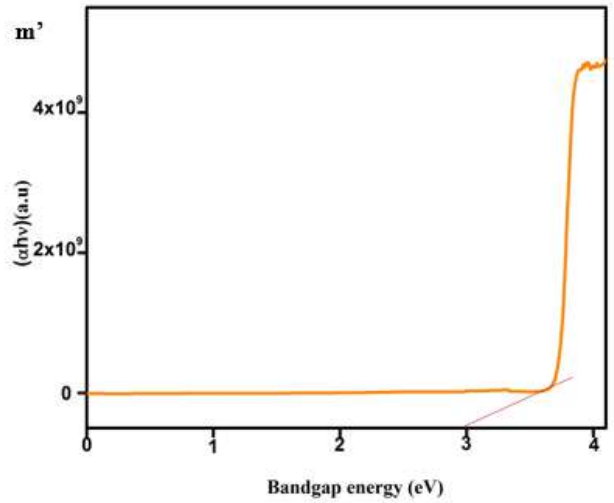

Figure 7.3 *UV-visible spectra of m') K (I) complex*

7.3.4 TG-DTA

i) [M($C_2H_8N_4O_3$)$_2$ {$C_{10}H_7$(1COO)}$_2$.2H_2O] where M= Mn (II), Ni (II), Co (II)Cu (II), Cd (II), Ca (II)

The thermal behavior of the complexes was studied using TG-DTA techniques and shown in **Figure 7.4**. The thermogram shows a three-step degradation process for most of the compound. In the first step, the degradation occurs at 100 °C and there is a weight loss of 36 %, due to the loss of water [M($C_2H_8N_4O_3$)$_2${$C_{10}H_7$(COO)}$_2$]. The second phase of

degradation is between 276 °C - 376 °C and an unstable intermediate [M{$C_{10}H_7(COO)$}$_2$] was obtained. Then the final stage of degradation happened at a temperature ranging from 441°C to 600 °C, at which the complexes eliminated the organic parts by leaving the metal oxides as a final residue, which was illustrated in **scheme (1)**.

Thermal decomposition scheme (1)

$[M(C_2H_8N_4O_3)_2\{C_{10}H_7(1\text{-}COO)\}\ 2H_2O] \xrightarrow{100\text{-}276\ ^0C} [M(C_2H_8N_4O_3)_2\{C_{10}H_7(1\text{-}COO)\}_2]\text{-}2H_2O$

$[M(C_2H_8N_4O_3)_2\{C_{10}H_7(1\text{-}COO)\}_2] \xrightarrow{276\text{-}376\ ℃} [M\{C_{10}H_7(1\text{-}COO)\}_2] - C_2H_8N_4O_3$

$[M\{C_{10}H_7(1\text{-}COO)\}_2] \xrightarrow{441\text{-}600\ ^\circ C} [MO]$

ii) [M($C_2H_8N_4O_3$)$_2$ {$C_{10}H_7$(1COO)}$_2$.2H_2O] where M= Zn (II), Sr (II), Ba(II), Li (I), Na (I), and K(I),

Figure 7.4 examines the TG-DTA weight loss that occurred in two steps in the temperature ranges from 230 °C to 600 °C. In the first phase, there is rapid ligand loss in the region from 230 to 395 °C, with a strong exothermic peak. In the second phase, there is an endothermic degradation around 400°C where the unstable intermediate is formed and finally results in the metal oxide formation, illustrated in **scheme (2),** and **Table 7.4**

Thermal decomposition scheme (2)

$[M(C_2H_8N_4O_3)_2\{C_{10}H_7(1\text{-}COO)\}\ H_2O] \xrightarrow{230\text{-}395\ ^0C} [M(C_2H_8N_4O_3)_2\{C_{10}H_7(1\text{-}COO)\}_2]\text{-}H_2O$

$[M(C_2H_8N_4O_3)_2\{C_{10}H_7(1\text{-}COO)\}_2] \xrightarrow{395\text{-}485\ ℃} [MO]$

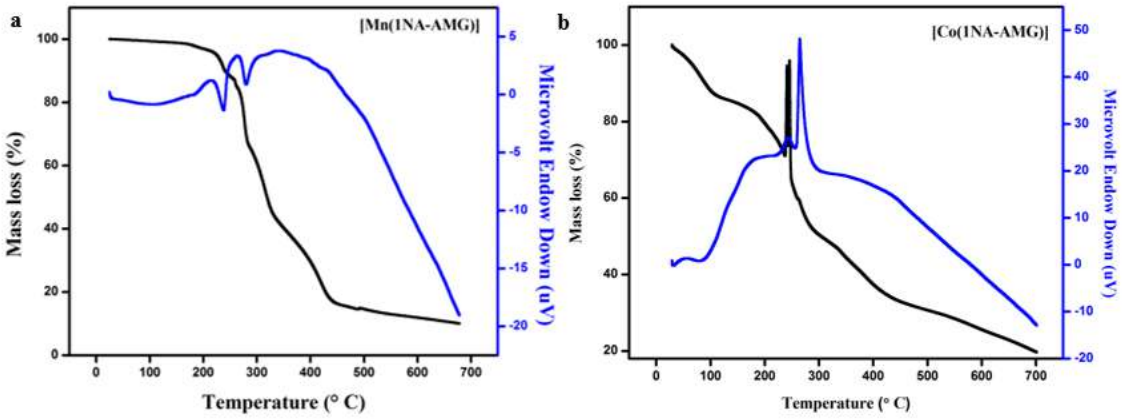

Figure 7.4 *TG-DTA curve of a) Mn(II) b) Co(II) complex*

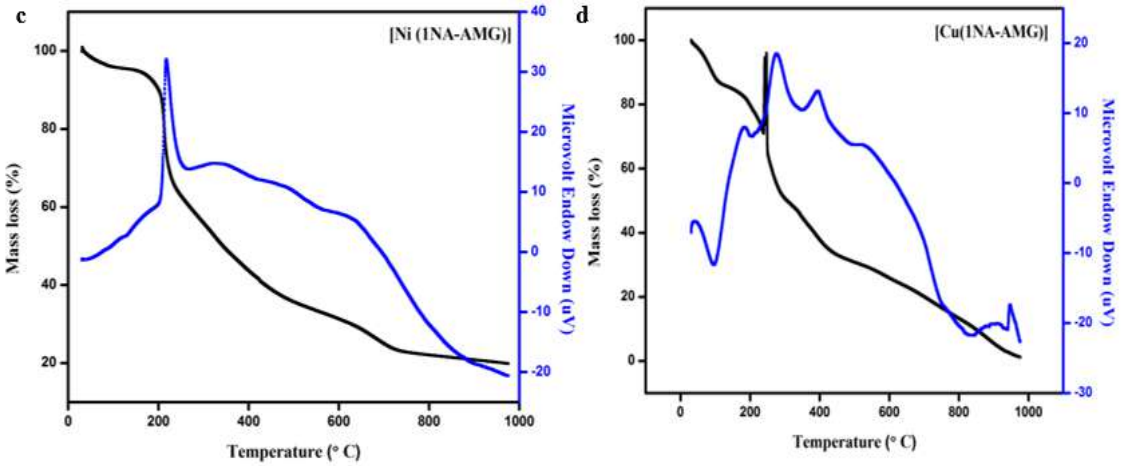

Figure 7.4 *TG-DTA curve of c) Ni (II) d) Cu (II) complex*

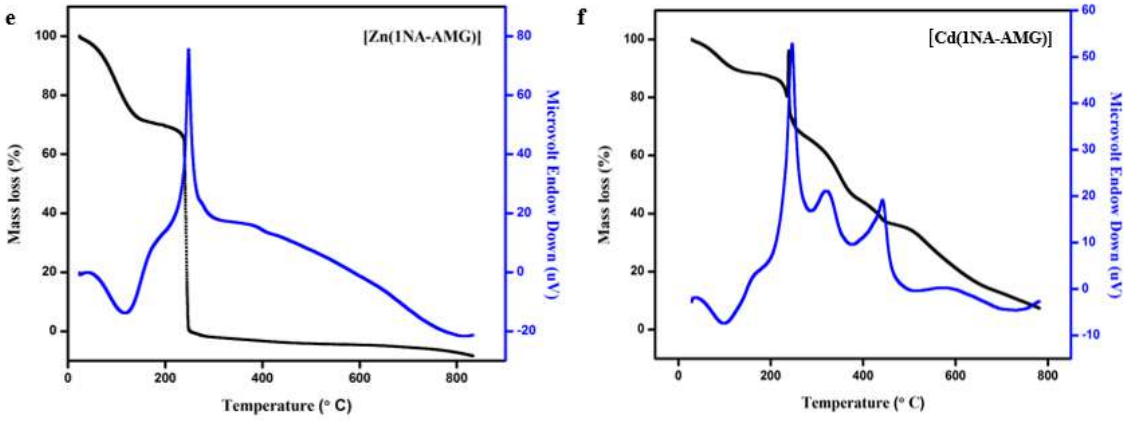

Figure 7.4 *TG-DTA curve of e) Zn (II) f) Cd (II) complex*

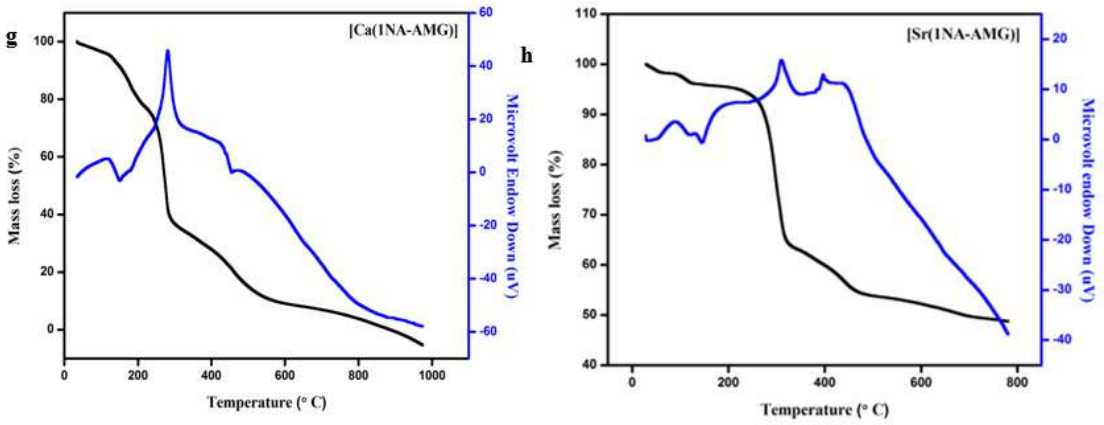

Figure 7.4 *TG-DTA curve of g) Ca(II) h) Sr (II) complex*

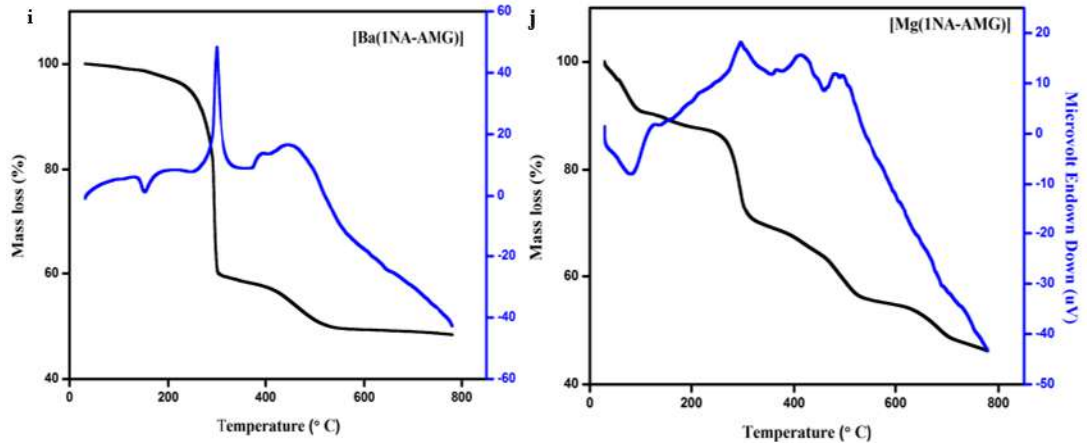

Figure 7.4 *TG-DTA curve of i) Ba (II) j) Mg (II) complex*

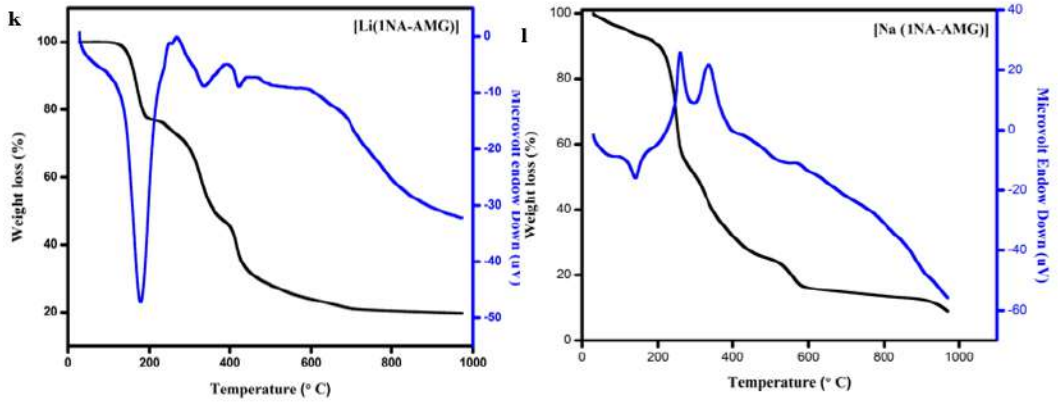

Figure 7.4 *TG-DTA curve of k) Li(I) l) Na(I)) complex*

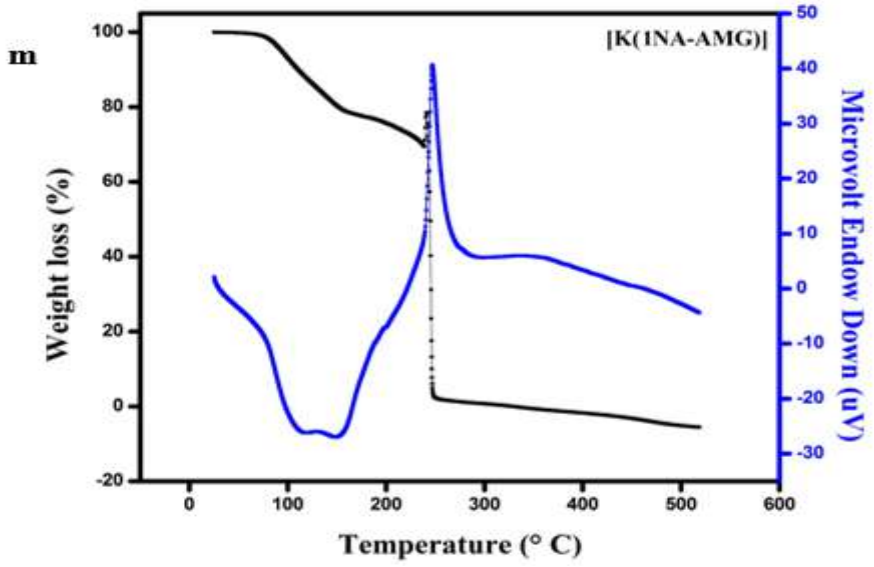

Figure 7.4 *TG-DTA curve of m) K(I) complex*

Table 7.4 *Thermal Analysis*

Metal complexes	DTA peak	Thermogravimetry			Decomposition Nature of the compound
		Temp Range(°C)	Weight loss (%)		
			Obsd.	Calcd.	
[Mn($C_2H_8N_4O_3$)$_2$ {$C_{10}H_7$(1-COO)}$_2$.2H $_2$O]	(+) 230, (+) 310	55-350	80	90	Dehydration and partial decomposition
	(-) 410	350-700	100	100	Complete decomposition to MnO_2
[Co($C_2H_8N_4O_3$)$_2$ {$C_{10}H_7$(1-COO)}$_2$.2H $_2$O]	(+) 110, (+) 315	100-320	90	90	Loss of water molecules
	(-) 299, (-) 300	360-600	100	100	Complete decomposition to metal oxide
[Ni($C_2H_8N_4O_3$)$_2$ {$C_{10}H_7$(1-COO)}$_2$.2H $_2$O]	(+) 210	55-250	80	90	Dehydration, Decomposition
	(-) 250, (-) 399	260-500	100	100	Completely decomposition to NiO
[Cu($C_2H_8N_4O_3$)$_2$ {$C_{10}H_7$(1-COO)}$_2$.2H $_2$O]	(+) 115, (+) 215	100-250	90	90	Partial Decomposition
	(-) 220, (-) 400, (-) 450	260-600	100	100	Complete formation of ZnO

Metal complexes	DTA peak	Thermogravimetry			Decomposition Nature of the compound
		Temp Range(°C)	Weight loss (%)		
			Obsd.	Calcd.	
[Cd($C_2H_8N_4O_3$)$_2$ {$C_{10}H_7$(1-COO)}$_2$.2H $_2$O]	(+) 101, (+) 399	100-400	70	80	Partial decomposition
	(-) 300, (-) 345, (-) 425	410-500	100	100	Formation of CdO
[Zn($C_2H_8N_4O_3$)$_2$ {$C_{10}H_7$(1-COO)}$_2$.2H $_2$O]	(+) 150	55-300	80	90	Decomposition
	(-) 350	320-500	100	100	Formation of ZnO
[Ca($C_2H_8N_4O_3$)$_2$ {$C_{10}H_7$(1-COO)}$_2$.2H $_2$O]	(+) 200, (+) 399	100-400	90	100	Decomposition of a compound
	(-) 300, (-) 425	420-700	100	100	Complete decomposition to CaO
[Sr($C_2H_8N_4O_3$)$_2$ {$C_{10}H_7$(1-COO)}$_2$.2H $_2$O]	(+) 210, (+) 395	100-400	90	90	Decomposition of an organic compound
	(-) 399, (-) 425	425-600	100	100	Complete decomposition to metal oxide
[Ba($C_2H_8N_4O_3$)$_2$ {$C_{10}H_7$(1-COO)}$_2$.2H $_2$O]	(+) 74, (+) 150	55-166	85	90	Melting and dehydration
	(-) 399, (-) 425	166-600	100	100	Complete decomposition to metal oxide
[Mg($C_2H_8N_4O_3$)$_2$ {$C_{10}H_7$(1-COO)}$_2$.2H $_2$O]	(+) 160	55-200	80	80	Loss of water molecules
	(-) 365, (-) 399, (-) 589	250-600	100	100	Complete decomposition MgO
[Li($C_2H_8N_4O_3$)$_2$ {$C_{10}H_7$(1-COO)}$_2$.2H $_2$O]	(+) 200, (+) 310	110-325	90	90	Decomposition of an organic moiety
	(-) 425	325-600	100	100	Complete decomposition to metal oxide
[Na($C_2H_8N_4O_3$)$_2$ {$C_{10}H_7$(1-COO)}$_2$.2H $_2$O]	(+) 210,(+) 345	25-360	80	90	Partial decomposition
	(-) 362, (-) 400	360-600	100	100	Decomposition to metal oxide
[K($C_2H_8N_4O_3$)$_2$ {$C_{10}H_7$(1-COO)}$_2$.2H $_2$O]	(+) 110, (+) 150	30-300	80	90	Dehydration and partial decomposition
	(-) 310, (-) 365	350-600	100	100	Final residues as metal oxide

7.3.5 Powder -XRD for the metal complexes

The powder X-ray diffraction for the metal complexes was recorded and exhibited in **Figure 7.5**. The individual peaks of the complexes are identified with the support of software from LSUCRPC. 2θ, D(space), and FWHM size (°) was calculated and presented in **Table 7.5**. The powder diffractogram suggests the crystalline and isomorphous nature of the metal complexes.

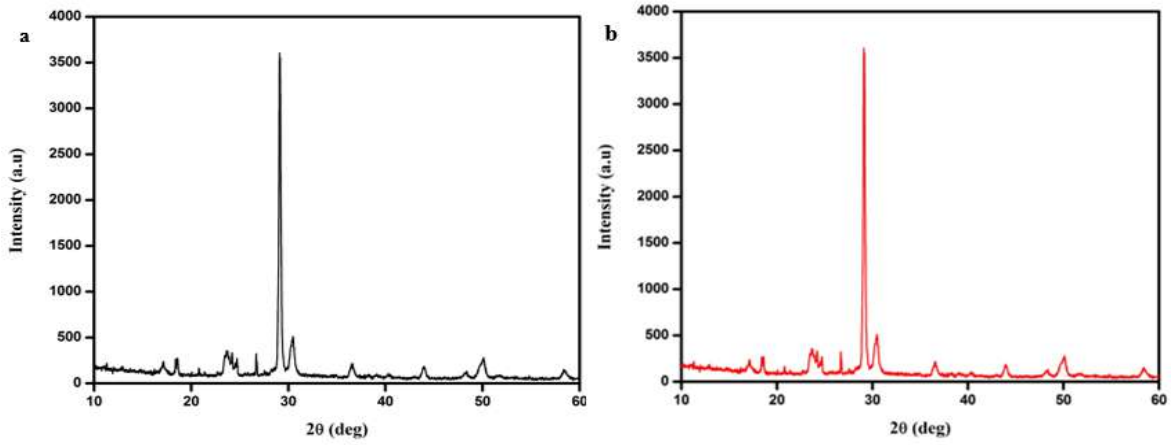

Figure 7.5 *XRD peak of a) Mn II) b) Co (II) complex*

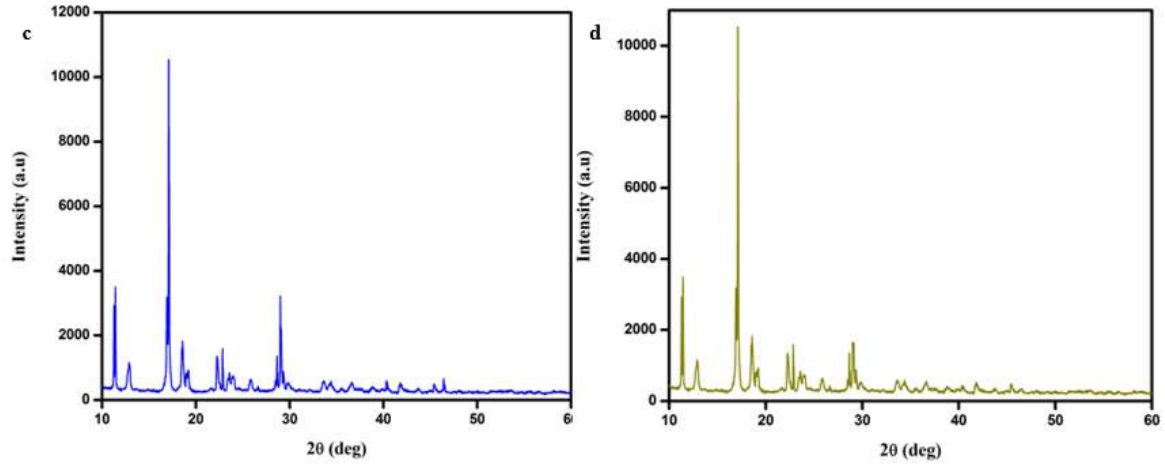

Figure 7.5 *XRD peak of c) Ni (II) d) Cu (II) complex*

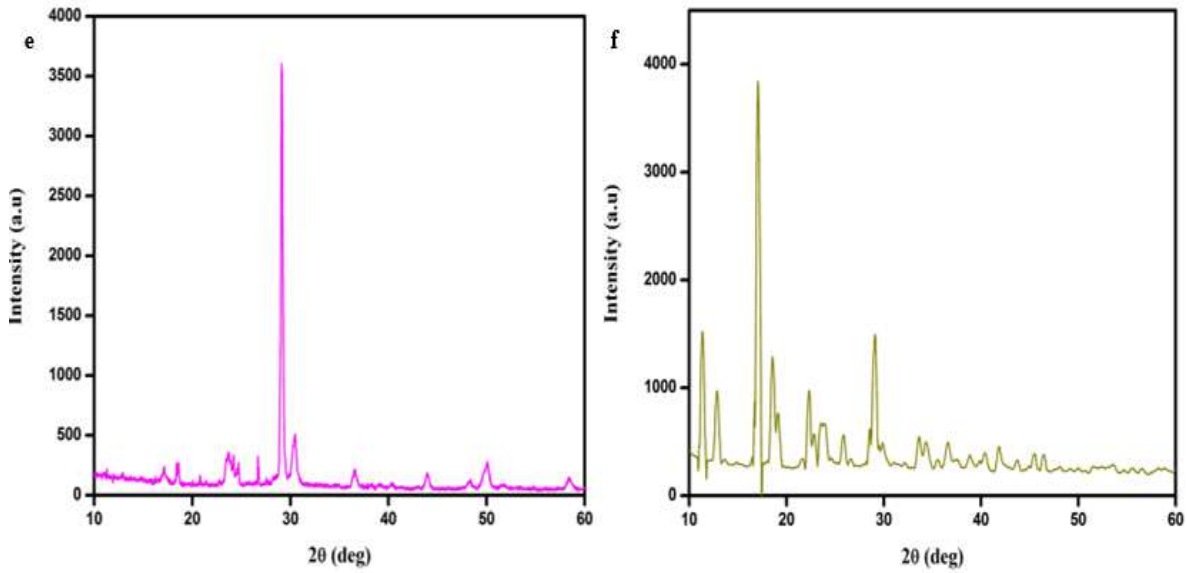

Figure 7.5 *XRD peak of e) Zn (II) f) Cd (II) complex*

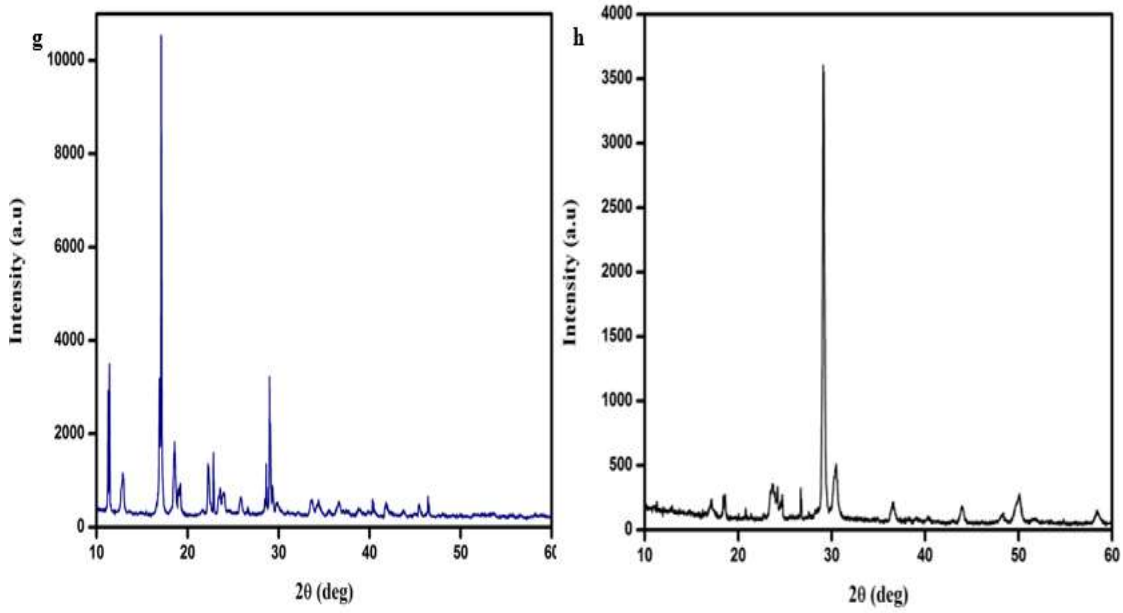

Figure 7.5 *XRD peak of g) Ca (II) h) Sr (II) complex*

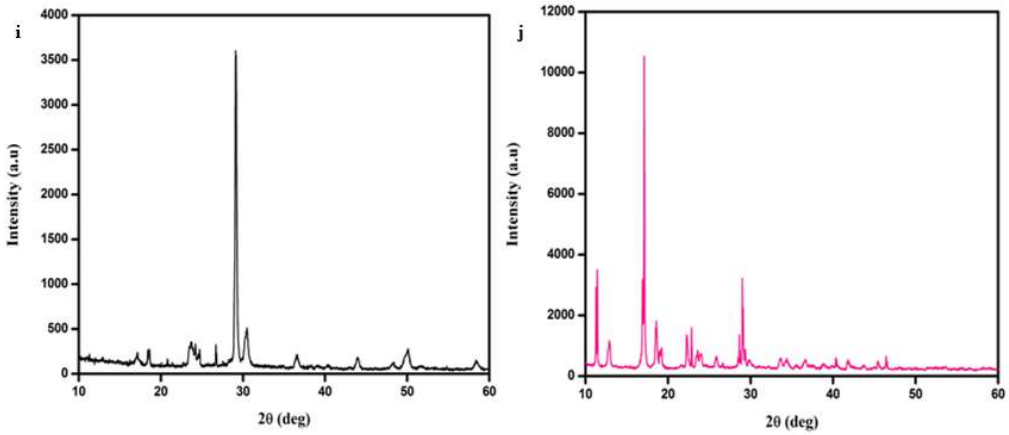

Figure 7.5 *XRD peak of i) Ba (II) j) Mg (II) complex*

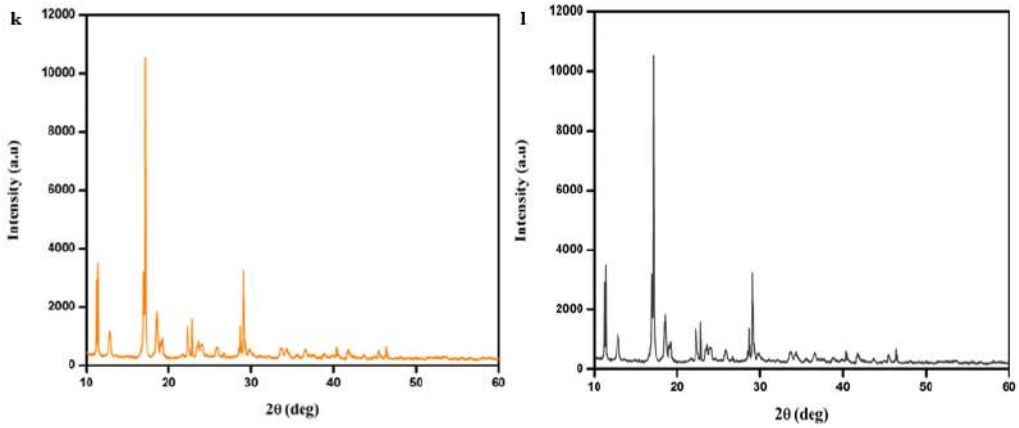

Figure 7.5 *XRD peak of k) Li(I) l) Na (I) complex*

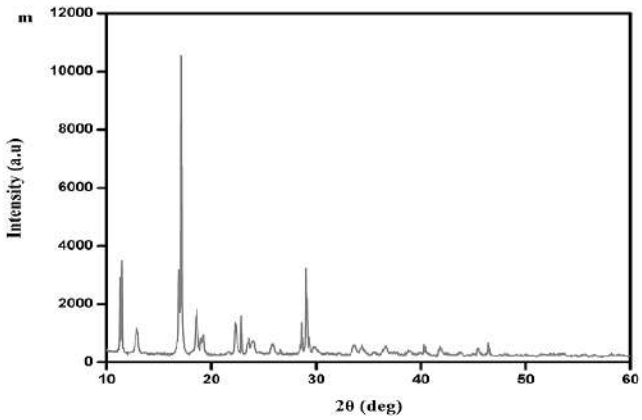

Figure 7.5 *XRD peak of m) K(I) complex*

Table 7.5 *P-XRD pattern for metal complexes*							
Complex	**2θ**	**FWHM B_{size} (°)**	**D(space)**	**Complex**	**2θ**	**FWHM B_{size} (°)**	**D(space)**
$[Mn(C_2H_8N_4O_3)_2\{C_{10}H_7(1\text{-}COO)\}_2.2H_2O]$	16.1	0.461	18.19	**$[Sr(C_2H_8N_4O_3)_2\{C_{10}H_7(1\text{-}COO)\}_2.2H_2O]$**	12.5	0.461	18.12
	19.4	0.469	17.96		16.1	0.469	17.88
	21.46	0.463	18.25		19.2	0.463	18.19
	27.22	0.502	17.02		24.76	0.502	16.94
	29.59	0.565	15.20		26.71	0.565	15.11
$[Co(C_2H_8N_4O_3)_2\{C_{10}H_7(1\text{-}COO)\}_2.2H_2O]$	13.85	0.461	18.14	**$[Ba(C_2H_8N_4O_3)_2\{C_{10}H_7(1\text{-}COO)\}_2.2H_2O]$**	12.5	0.461	18.12
	19.09	0.469	17.95		16.1	0.469	17.88
	22.49	0.463	18.29		19.2	0.463	18.19
	27.75	0.502	17.04		24.76	0.502	16.94
	31.03	0.565	15.25		26.71	0.565	15.11
$[Ni(C_2H_8N_4O_3)_2\{C_{10}H_7(1\text{-}COO)\}_2.2H_2O]$	12.61	0.461	18.12	**$[Mg(C_2H_8N_4O_3)_2\{C_{10}H_7(1\text{-}COO)\}_2.2H_2O]$**	12.82	0.461	18.13
	16.42	0.469	17.89		16.1	0.469	17.88
	18.88	0.463	18.18		18.88	0.463	18.18
	23.2	0.502	16.89		24.86	0.502	16.94
	26.51	0.565	15.10		26.71	0.565	15.11
$[Cu(C_2H_8N_4O_3)_2\{C_{10}H_7(1\text{-}COO)\}_2.2H_2O]$	12.09	0.461	18.11	**$[Li(C_2H_8N_4O_3)_2\{C_{10}H_7(1\text{-}COO)\}_2.2H_2O]$**	12.40	0.461	18.12
	16.01	0.469	17.88		16.22	0.469	17.88
	19.09	0.463	18.19		19.22	0.463	18.19
	21.87	0.502	16.85		25.01	0.502	16.94
	27.02	0.565	15.12		27.78	0.596	14.35
$[Zn(C_2H_8N_4O_3)_2\{C_{10}H_7(1\text{-}COO)\}_2.2H_2O]$	12.5	0.461	18.12	**$[Na(C_2H_8N_4O_3)_2\{C_{10}H_7(1\text{-}COO)\}_2.2H_2O]$**	12.43	0.461	18.12
	16.1	0.469	17.88		16.22	0.469	17.88
	19.2	0.463	18.19		19.22	0.463	18.19
	23.41	0.502	16.89		25.02	0.502	16.94
	26.6	0.565	15.10		27.77	0.596	14.35
$[Cd(C_2H_8N_4O_3)_2\{C_{10}H_7(1\text{-}COO)\}_2.2H_2O]$	12.2	0.461	18.11	**$[K(C_2H_8N_4O_3)_2\{C_{10}H_7(1\text{-}COO)\}_2.2H_2O]$**	12.44	0.461	18.12
	16.21	0.469	17.88		16.22	0.469	17.88
	18.99	0.463	18.18		19.22	0.463	18.19
	24.76	0.502	16.94		25.02	0.502	16.94
	26.4	0.565	15.10		27.78	0.596	14.35
	27.84	0.596	14.35		12.44	0.461	18.12

7.3.6 Antimicrobial activity

The antibacterial efficiency of the metal complexes Ni (II), Co (II), Cu (II), and Zn (II) was investigated using the disc diffusion method. The antibacterial activity against *Staphylococcus aureus* and *Escherichia coli* is shown in **Table 7.6** and **Figure 7.6, 7.7,** along with inhibition zone of the metal complexes. Zn (II) exhibits the highest levels of inhibition (12 mm and 18 mm, respectively) against *Staphylococcus aureus* and *Escherichia coli* among the metal complexes.

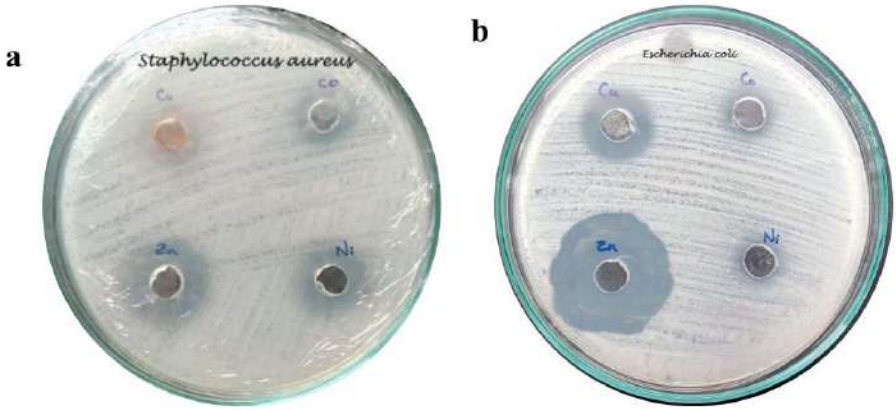

Figure 7.6 *Antimicrobial activity of the Zn (II) complex against a) Staphylococcus aureus b) Escherichia coli*

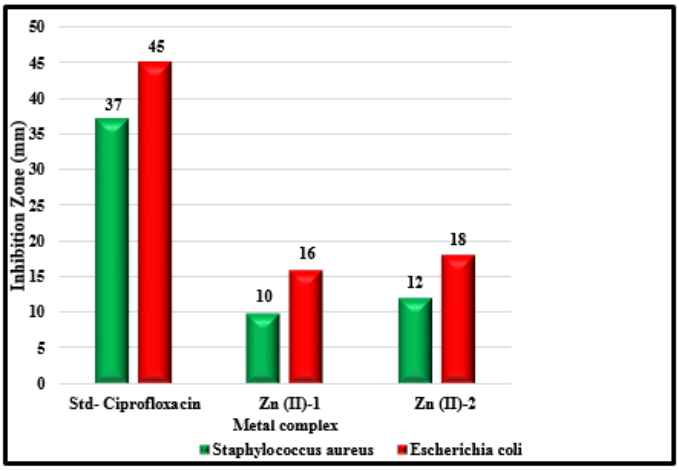

Figure 7.7 *Inhibition evaluation of the Zn (II) complex against bacteria*

Table 7.6 *Antibacterial Activity*		
Compound	**Inhibition zone (mm) (100µg/disc)**	
	Staphylococcus aureus	***Escherichia coli***
Standard – Ciprofloxacin	37	45
Zn(II)-1	10	16
Zn (II)-2	12	18

7.3.7 Anticancer Activity

Human breast cancer cells (MCF-7) and human lung cancer cells (A549) are the two categories of cell lines used to study the cytotoxicity activity of the zinc (II) complex. The control used for study is cisplatin. The formula for calculating percentage viability is shown in Eq.**(7.2).**

$$\%\ viability = \frac{OD\ value\ of\ Zn\ (II)\ complex}{OD\ value\ of\ control\ (\text{Cisplatin})} X100 \qquad \textbf{Eq.(7.2)}$$

A plot of concentration vs. percentage cell viability determines the inhibitory activity of the cancer cells. According to the graph, breast cancer cells are destroyed at a concentration of 28 ± 0.7 g/ml and lung cancer cells at a concentration of 25± 1.2g/ml. **Table 7.7** displays the zinc (II) complex's coefficient of inhibition. The microscopic image of cancer cells are seen in **Figures 7.8 (a, b)**, and **Figures 7.9 (a, b)** show the cytotoxicity activity. The inhibition of cell viability is not seen when the concentration of the complex increases. This reveals that, only at lower concentrations, the zinc complex is highly cytotoxic to breast cancer cells (MCF-7) and lung cancer cells (A549).

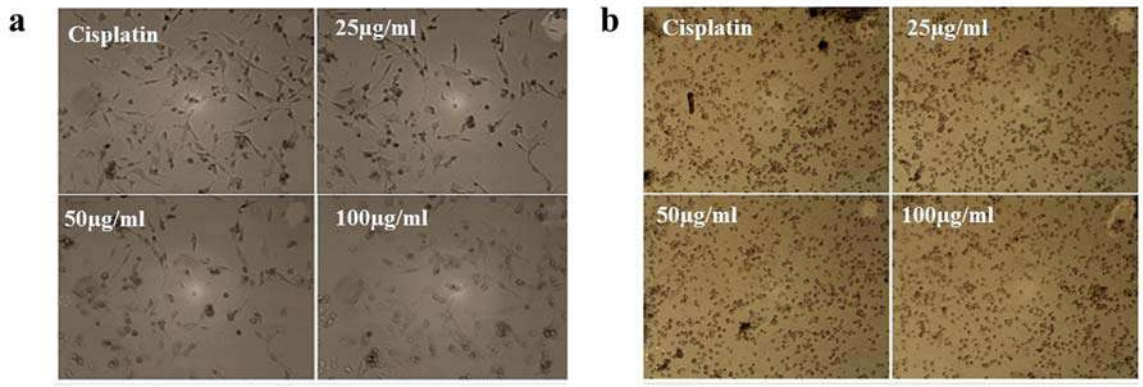

Figure 7.8 *Microscopy images of a) breast cancer cells and b) lung cancer cells*

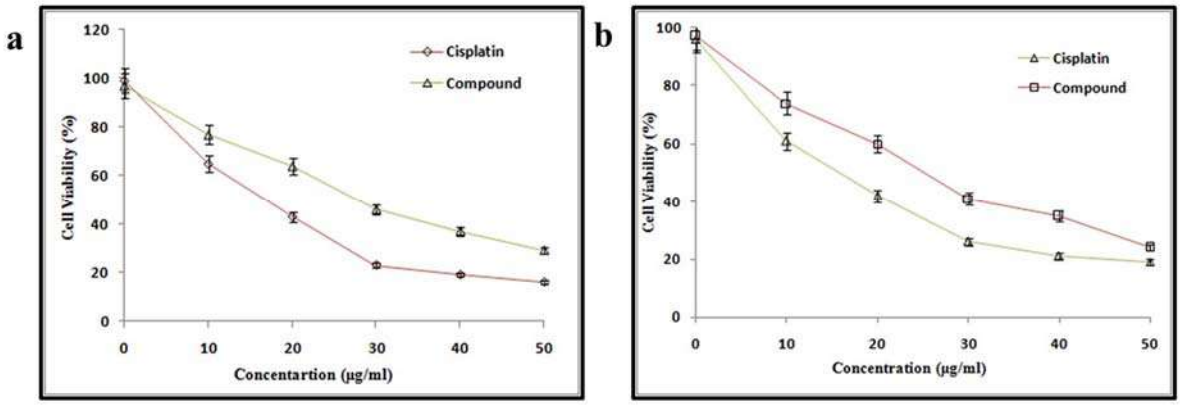

Figure 7.9 *Cytotoxicity graph of Zinc (II) complex in a) breast cancer cells and b) lung cancer cells*

Table 7.7 *Anticancer Assay*		
Compound (µM/ml)	**50% of inhibition (IC_{50}) (µg/ml)**	
	Human Breast cancer cell (MCF-7)	**Human lung cancer cell (A549)**
Zn (II)	28 ± 0.7	25± 1.2
Control – Cisplatin	13 ± 1.8	12 ±1.0

7.4 ENERGY APPLICATION OF METAL COMPLEXES ON Ca^{2+}, Sr^{2+}, Ba^{2+}, Li^{+}, Na^{+}, and K^{+}

7.4.1 LSV studies

The electrocatalytic performance of the catalyst was analyzed by LSV technique using a three-electrode system dipped in 0.5 M sulphuric acid at a scan rate of 5 mV s^{-1}. In the LSV curves shown in **Figure 7.10a**, their cathodic currents start from 3.8 V, accompanied by hydrogen absorption and evolution. It was evident that the hydrogen evolution potential is positive for alkaline earth metals. Lithium electrocatalyst shows higher cathodic current density at 3.8 V, directly proportional to the potential of HER. Interestingly, from **Figure 7.10b,** except the barium electrocatalyst, all others produce a current density of 10 mA cm^{-2} at minimal overpotential in the 20- 25 mV range, which is equivalent to the overpotential required for solar fuel production **(Table 7.8).** In the attainment of 40 mA cm^{-2}, the same order follows, except barium, all other catalyst generates lower overpotential . The higher HER activity of the lithium electrocatalyst may be sustained due to the strong ligand effect on the metal ion, thereby modifying the metal's electronic structure.

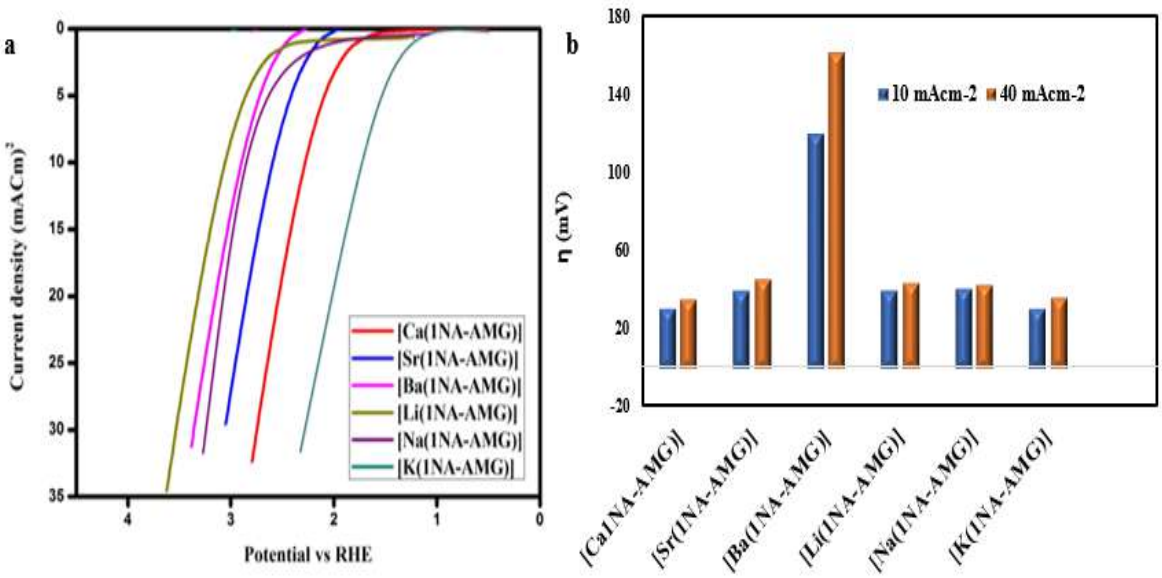

Figure 7.10. *a) LSV analysis results for synthesized electrocatalyst towards HER b) Overpotential obtained at a current density of 10 and 40 $mAcm^{-2}$*

Table 7.8 *Electrocatalytic efficiency of synthesized catalyst towards HER electrocatalyst medium overpotential.*	
Catalyst	**Overpotential mA/cm^2(mV)**
[Ca($C_2H_8N_4O_3$)$_2$ {C_{10}H7(1-COO)}$_2$.2H $_2$O]	93
[Sr($C_2H_8N_4O_3$)$_2$ {C_{10}H7(1-COO)}$_2$.2H $_2$O]	78
[Ba($C_2H_8N_4O_3$)$_2$ {C_{10}H7(1-COO)}$_2$.2H $_2$O]	71
[Mg($C_2H_8N_4O_3$)$_2$ {C_{10}H7(1-COO)}$_2$.2H $_2$O]	135.85
[Li($C_2H_8N_4O_3$)$_2$ {C_{10}H7(1-COO)}$_2$.2H $_2$O]	84
[Na($C_2H_8N_4O_3$)$_2$ {C_{10}H7(1-COO)}$_2$.2H $_2$O]	92

7.4.2 EIS studies

The EIS spectra were recorded to have better insight about the hydrogen evolution reaction and knowledge about electrode kinetics **(Figure 7.10c)**. It implies capacitive semicircle curves with a diverse radius for the examined cathodic electrodes. The spectra were recorded at varied cathodic potentials depending on potentiodynamic measurement results. A characteristic loop was observed for all the catalysts assigned to the adsorption of a notable quantity of hydrogen electrode layer. The charge transfer (R_{ct}) resistance for the [Li (2NA- AMG)] catalyst is smaller than the other catalyst, indicating the HER activity. We know that the hydrogen evolution rate is depends on R_{ct} value; the smaller the R_{ct} value higher the catalytic performance . The charge transfer process is primarily utilized to normalize the HERs activity and is shown by a single loop in Nyquist plots. The electrocatalyst's different charge transfer resistance shows the different hydrogen deposition ratios on the catalyst. This phenomenon might be ascribed to the electrodes' size, shape, and composition disparity. So, the Li catalyst was enriched with active sites and found superior to other catalysts.

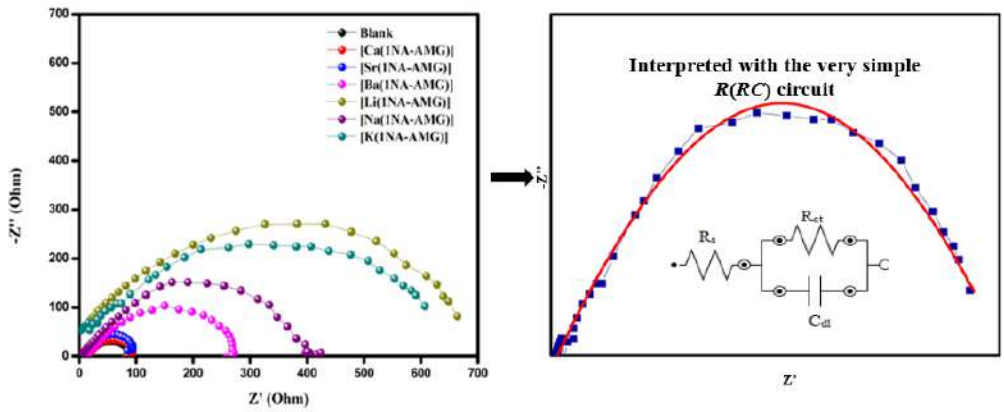

Figure 7.10. *c) EIS analysis for the circuit catalyst*

7.4.3 Butler–Volmer equation and Tafel curves

Charge transfer overpotentials were usually measured by the kinetics of heterogeneous electron transfer and calculated from Butler–Volmer equation [**Eq. (7.3)**] when the reactants are more significant than current, overpotential was negligible. In this equation, I am current, A is surface area, i_o is exchange current density, a is charge transfer barrier, n is the number of electrons engaged in the process, and η_{act} is charge transfer overpotential.

$$\boldsymbol{I = Ai_o\{e^{\alpha nF/RT}\,\eta - e^{(1-\alpha)nF/RT}\,\eta\}} \qquad \textbf{Eq. (7.3)}$$

Standard electrodic process takes place in multiplies in the elementary step, by association with overpotential in each and every step. The i_o is a vital parameter that decides the oxidation/reduction reaction rate at equilibrium; a fast reaction was engaged with high io, whereas a slow reaction with a low i_o value. The simplified butler-Volmer equation is known as the Tafel equation, shown in **Eq. (7.4)**. The current density (i) and Tafel slope (b) are the two important factors to interrogate electrode reaction kinetics. A Plot of log i vs. overpotential is referred to as a Tafel Plot **(Figure 7.11a).** The Tafel plot Li catalyst shows a minimum Tafel slope of 6.38 mV/dec correlated with diverse catalysts, which has a slope in the range of 7.82-40 mV/dec. Impart with the Butler-Volmer equation, the progression between the Tafel and Heyrovsky mechanism pathway was recognized from variation in Tafel slopes. Precisely, the Tafel slopes calculated as per **Figure 7.11b,** 15.58, 18.36, and 27.86 mV/dec are designated into the Volmer, Heyrovsky, and Tafel as the kinetic steps. Thus, the Li electrocatalyst with the highest binding energy will have stronger hydrogen adsorption and barium has the most negligible adsorption, which in turn shows

the ability of alkali metals towards HER activity. Lithium catalyst improves the electrode performance by decreasing the energy barrier. Moreover, the porous structure of lithium provides more reaction sites and increases current density.

$$\eta_{act} = blog_{10}(\frac{i}{i_o}) \qquad \textbf{Eq. (7.4)}$$

Electrochemical impedance spectra are essential data to examine the physical and chemical processes inside the electrode. It is possible to determine the stability and kinetics of the system at the solid-solid interface and solid-liquid interface. Both Nyquist plots and Bode plots are equally essential, but the Nyquist plots failed to give the data about magnitude. In the Bode plot, the graph was plotted between magnitude vs. frequency **(Figure 7.11c)**.

Further, a bode plot was derived for all the catalysts to study the enhancement of HER activity. With the increase in frequency, the diameter of the semicircle reduced accordingly. The decreased value of relaxation time indicates the porous nature of the catalyst. Comparatively, the relaxation time of lithium is lesser, which leads to the fact that the amorphous nature of the catalyst will increase the space between electrode and electrolyte, thus initiating the mass transfer throughout the electrochemical process. The large ionic conductivity of Li^+ in the range of 10^{-3} to 10^{-1} S cm^{-1} will also increase the charge transfer reaction.

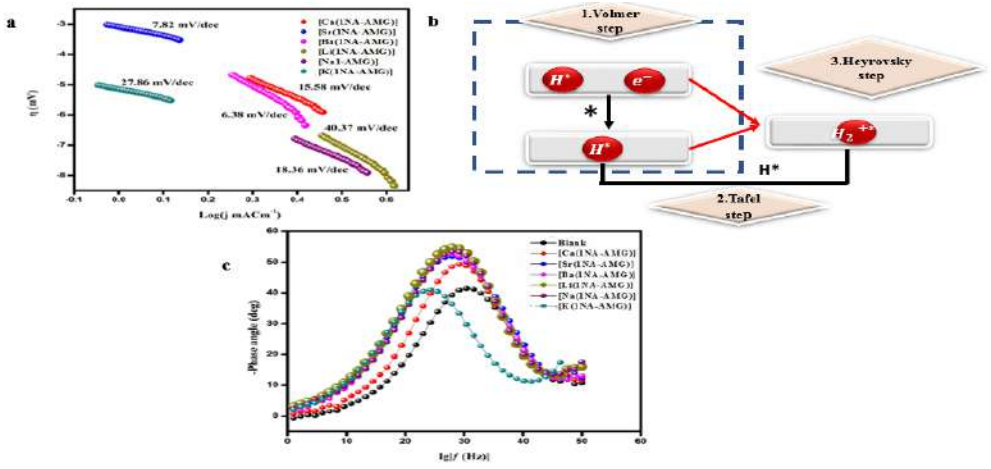

Figure 7.11*a) Tafel slopes of the electrocatalyst measured with the three-electrode system, b) HER mechanism of (Volmer &Tafel reaction), and c) Bode plot of electrocatalyst in 0.5 M H_2SO_4 at room temperature.*

7.4.4 Cyclic voltammetry

The mechanistic analysis of the electrode process involving oxidation/reduction half-cell reactions will be understood clearly from cyclic Volta graphic techniques. For a perfect electrochemical reversible system, the value of peak currents should be 1 with consistent potential separations of 60 mV/n, where n is the number of electrons engaged in the process. In our targeted catalyst, except barium and potassium, all others show single peaks for oxidation and reduction reactions. Multiplex peaks in the CV of Ba^{2+} and K^{+} is probably due to multi-step parallel/consecutive process with numerous steps or due to different redox process.

The attributes of cyclic voltammetry are controlled by several factors like electrode surface, electron transfer reactions, the nature of the species, their diffusion, and the sweep rate. From **Figure 7.12**, the reduction peak current density for electrodes A, B, and C is about -0.3V, -0.2V, +0.1V, +0.5V, +0.2V, and +0.1V, respectively. Correlating with other catalysts, lithium-ion shows more cathodic current potential with higher peak height. The downward peak may be due to the reduction of Li^{+} to $Li^{0,}$ and the upward peak is due to the oxidation of metal ions. This is the suggested reaction scheme of the lithium complex in acidic media. No apparent oxidation peaks are seen, implying that lithium-ion is the suitable candidate with more excellent stability. The in-depth analysis of the redox process and peak separation of Li-ion was studied by using CV at diverse scan rates of 20- 120 mV/s, as shown in **Figure 7.13a**. A redox peak is seen at 0.5V and 1.2V along with one-plateau discharge curve. In all complexes, a uniform pattern of the redox process was pronounced, leading to identical CV curves. All the electrocatalyst follows quasi-reversible processes, which is affirmed by an increase in peak potential with an increase in scan rate.

The electrocatalyst's electrochemical surface area (ECSA) analysis helped to compare the stability. It was displayed in **Figure 7.13b**. It was evaluated by integrating the area under the peak linked with the reduction area. Finally, the proportion of electrochemically active sites in the redox process was assessed. By dividing this value by the normalization value, it yields catalyst ECSA.

The ECSA of Li was found to be 0.3777 cm^{-2}, greater than reported alkali metals. Generally, an electrode with more significant electrochemically active sites will show greater ECSA value and perform excellent HER activity [60]. Greater nucleation and linear plot for the Li electrocatalyst show its enhanced capacity and occurrence of large catalytically active sites in the surface represented in **Table 7.9**.

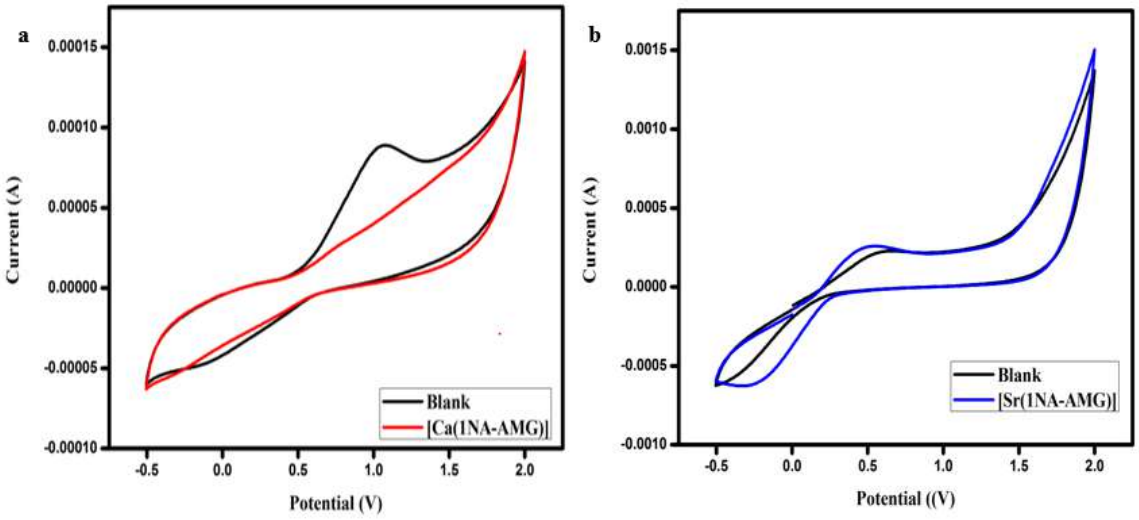

Figure 7.12 *Cyclic voltammetry curves a) Ca (II) b) Sr (II) at a scan rate of 100 of* mVs^{-1}

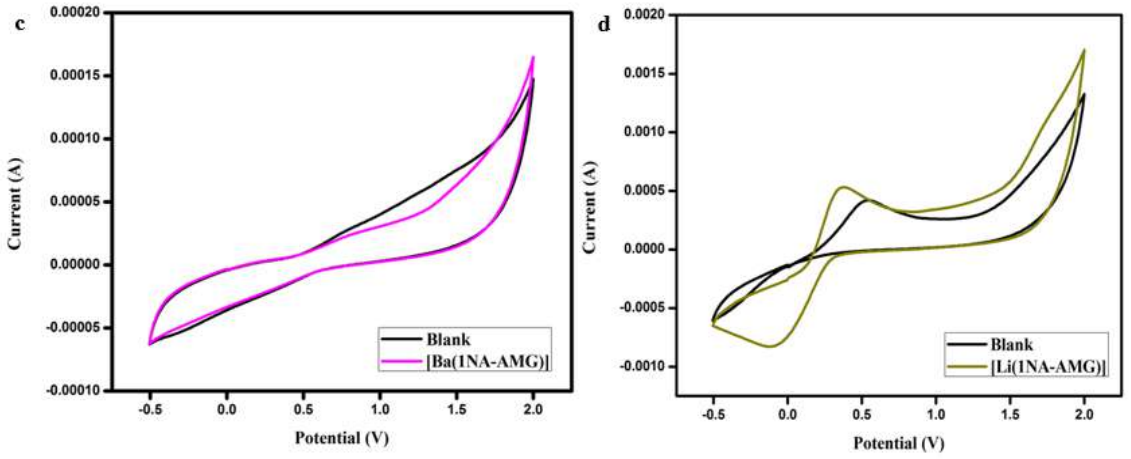

Figure 7.12 *Cyclic voltammetry curves c) Ba (II) d) Li (II) at a scan rate of 100 of* mVs^{-1}

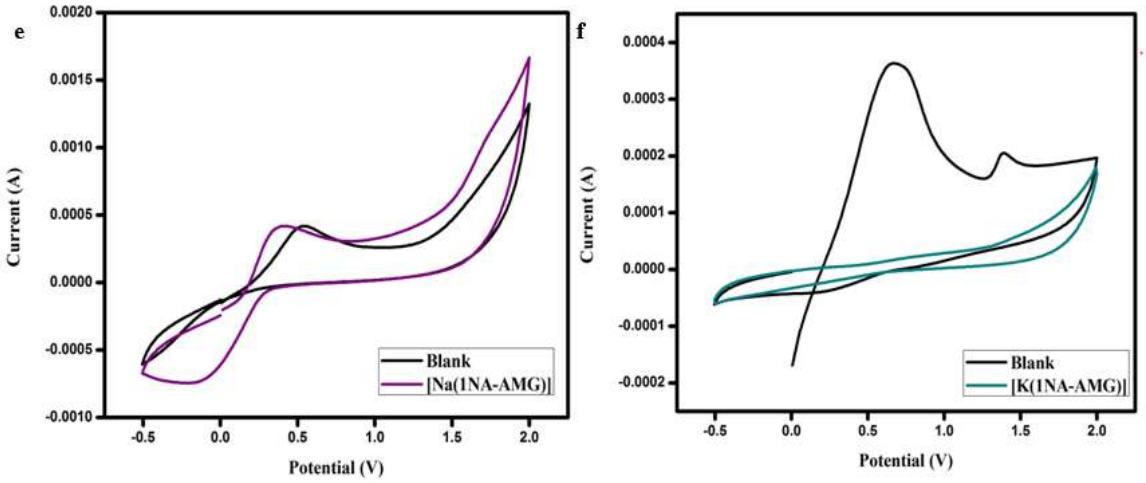

Figure 7.12 *Cyclic voltammetry curves e) Na (II) f) K (II) at a scan rate of 100 of mVs^{-1}*

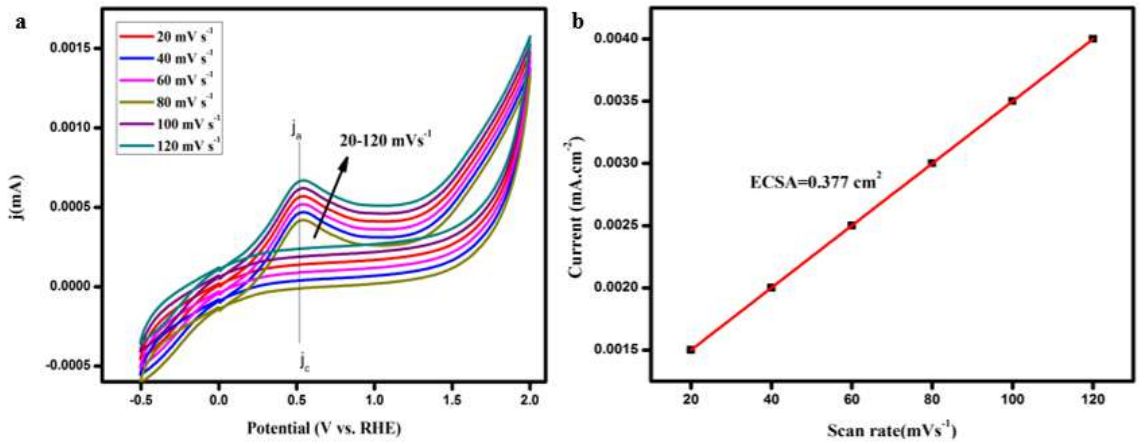

Figure 7.13 *a) Cyclic voltammogram for lithium catalyst at a scan rate of 20-120 mVs^{-1} b) Electrochemical surface area (ECSA) lithium plot.*

Table 7.9 *HER parameters of electrocatalyst in 0.5 H_2SO_4.*

Catalyst	Tafel Slopes (mV/dec)	R_{ct} (Ω cm^2)	C_{dl} (μFcm^2)	ECSA ($mAcm^{-2}$)
$[Ca(C_2H_8N_4O_3)_2$ $\{C_{10}H7(1\text{-}COO)\}_2.2H_2O]$	15.58	36.6	24.5	0.348
$[Sr(C_2H_8N_4$ $O_3)_2$ $\{C_{10}H7(1\text{-}COO)\}_2.2H_2O]$	7.82	22.7	26.7	0.319
$[Ba(C_2H_8N_4$ $O_3)_2$ $\{C_{10}H7(1\text{-}COO)\}_2.2H_2O]$	6.38	54.1	18.7	0.143

Catalyst	Tafel Slopes (mV/dec)	R_{ct} (Ω cm^2)	C_{dl} ($\mu F cm^2$)	ECSA ($mAcm^{-2}$)
$[Mg(C_2H_8N_4O_3)_2\{C_{10}H7(1\text{-}COO)\}_2.2H_2O]$	40.37	98.7	14.2	0.377
$[Li(C_2H_8N_4O_3)_2\{C_{10}H7(1\text{-}COO)\}_2.2H_2O]$	18.36	68.4	18.8	0.274
$[Na(C_2H_8N_4O_3)_2\{C_{10}H7(1\text{-}COO)\}_2.2H_2O]$	27.86	74.5	15.4	0.206
Rct is the charge transfer resistance; Cdl is the double–layer capacitance, ECSA is the exchange current density based on the calculated electrochemically active surface area.				

7.4.5 Gibbs and Volcano

The DFT approaches are used to calculate ΔG and shown in **Figure 7.14a**. Lower the ΔGH* value, higher will be the HER activity. Probably the hydrogen atoms are get assimilated on the surface of the Li ion and hence act as efficient catalyst. The kinetics of integral electron transfer engaged in the HER can be evaluated by the exchange current (i_0). Consequently, a volcano plot was drawn between i_0 vs ΔGH* to examine the quantitative evolution of hydrogen (**Figure 7.14d**). The electrocatalyst which occupies the peak at volcano plot will have maximum exchange current with remarkable HER activity. From the **Figure 7.14d**, it was clearly confirmed that Li act as efficient catalyst which lodges top position in the plot. Hydrogen adsorption in the electrode is the primary step in the HER process and it was investigated Li ion as effective catalyst. With the idea of understanding the kinetics of evolution reaction intensively, the hydrogen formation reaction was also studied and presented in **Figure 7.14f**. The hydrogen formation can occur in two possible ways: Heyrovsky or Tafel reaction. The barrier energy of Tafel reaction (2.831 eV) was higher than Heyrovsky reaction (2.364 eV). Thus, Heyrovsky reaction with lower energy is the predominant pathway for hydrogen production with lithium catalyst.

To confirm the efficacy of lithium electrocatalyst, a comparison analysis was made with other available electrocatalyst. For varied catalyst, different HER mechanism was followed. By keeping Pt as the standard catalyst, the kinetic behavior of Li was calculated. The values -0.91eV and 2.36 eV are ΔGH* value and HER kinetic barrier energy, respectively.

The two-dimensional volcano plot is shown in **Figure 7.14b**. The upper position of the volcano plot synchronizes to $\Delta G_0H = 0$; the strong binding of metal with a hydrogen atom is shown on the left side, and weak binding is shown on the right side of the peak.

The appropriate condition would be intermediate binding of metal with hydrogen, not too strong or weak. The activity of any metal can easily predict with the help of the ΔG_0 value.

Remarkably, the exchange current can also be represented by a volcano plot in three-dimensional view, as shown in **Figure 7.14c**. Since the highest exchange current found in when both ΔG_0 H(1) and ΔG_0 H(2) are equal to zero the hydrogen adsorption reaction was found to be thermoneutral in nature .

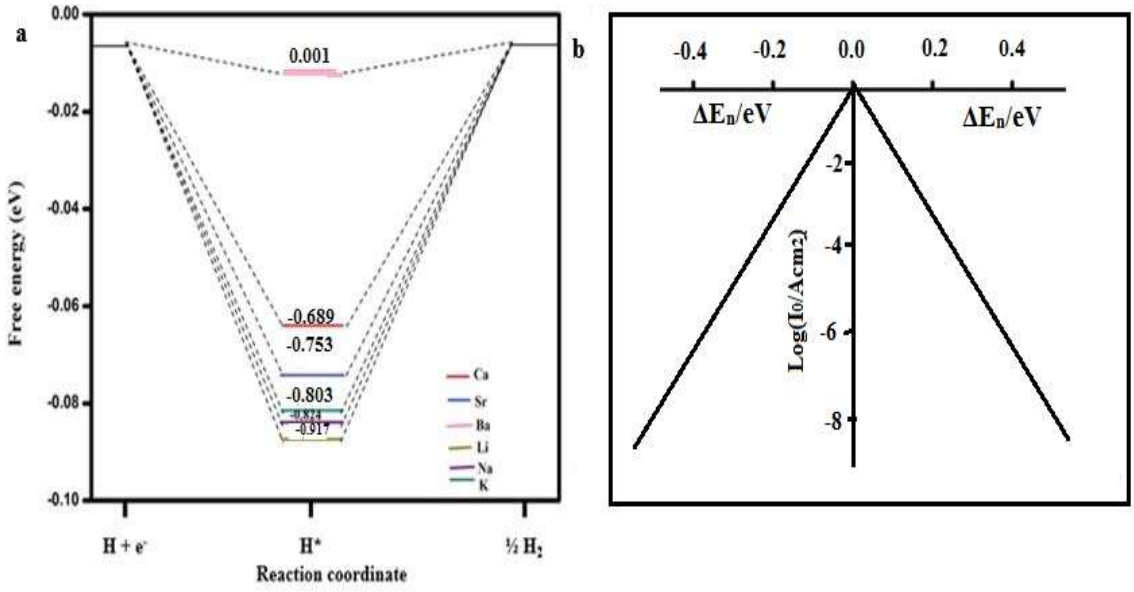

Figure 7.14. *a) Gibbs free energy diagram of the HER catalysts b) Two-dimensional volcano plot*

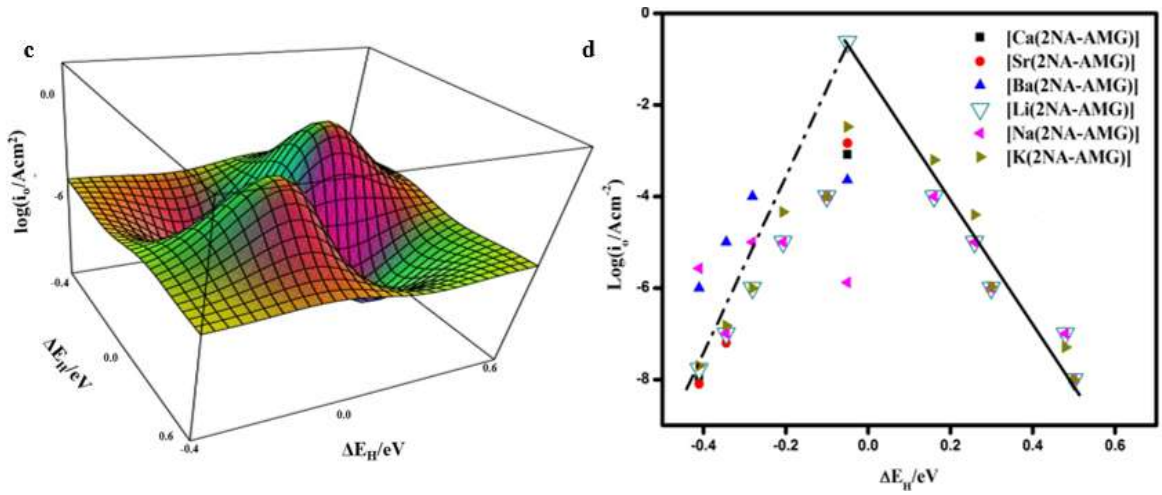

Figure 7.14. *c) Three-dimensional volcano plot d) Two-dimensional volcano plot*

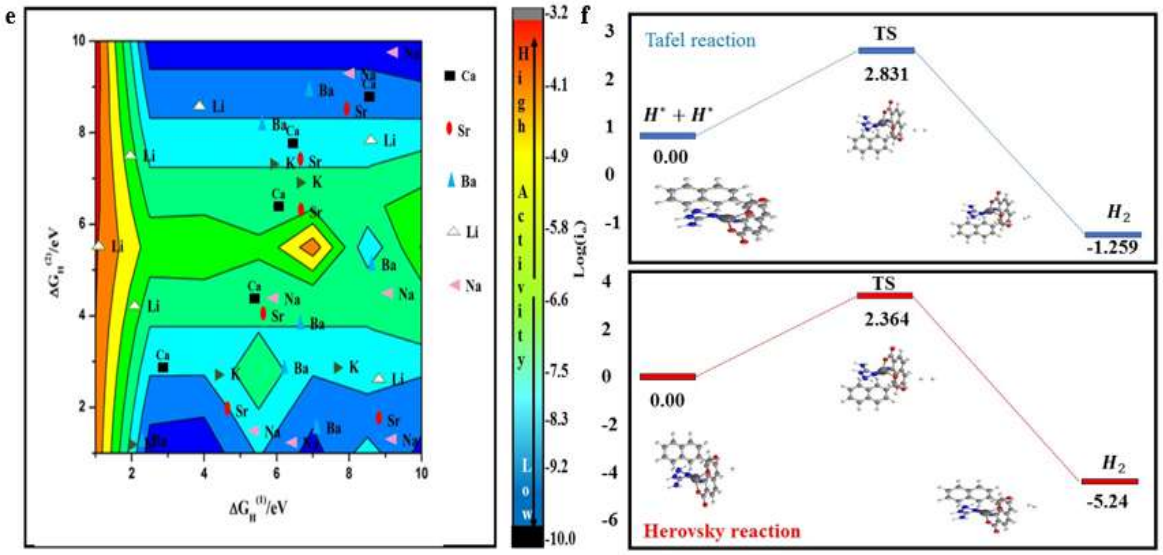

Figure 7.14. *e) Three-dimensional volcano plot showing activity electrocatalyst f) HER pathway through Heyrovsky reaction and Tafel reaction.*

7.4.6 Morphological of Lithium Catalyst

The SEM pictures of the Li catalyst are revealed in **Figure 7.15**, and the morphology of the electrocatalyst reveals bundled nature with a micro-scaled flower-like structure. The presence of voids between the flower will intensify the potent surface area of the electrode, thereby allowing the hydrogen atom to settle on its surface.

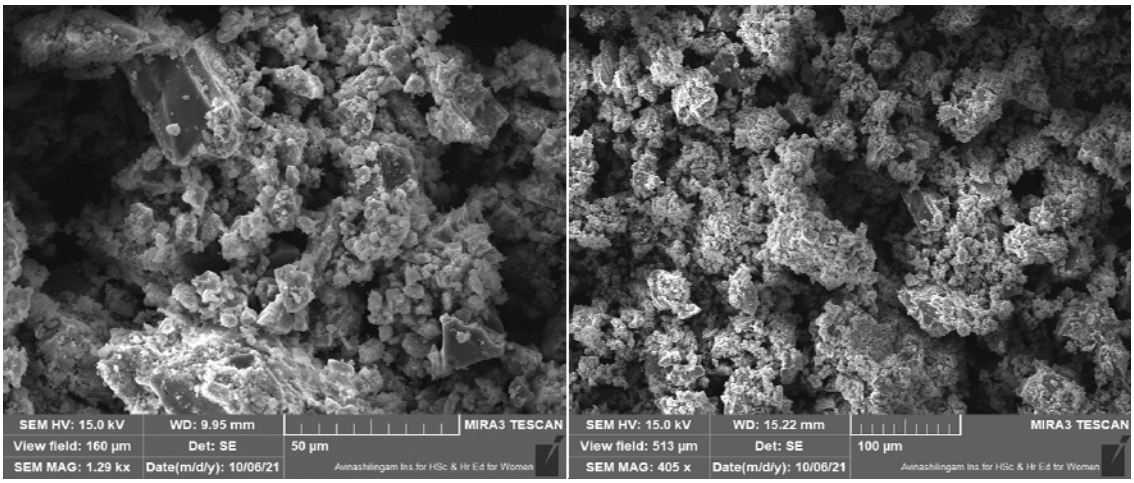

Figure 7.15 *SEM image of lithium catalyst 50 and 100 µm bar length.*

7.5 NANO-SIZED EPOXY- NiO, CoO, and $NiCO_2O_4$ NANOCOMPOSITES FOR ANTICORROSION APPLICATIONS

In the current study, we synthesized mixed metal complexes of Ni (II) and Co (II) by utilizing the bulky 1-naphthoic acid as the core element to assemble with aminoguanidine to prepare a oxide and mixed metal oxide The mixed metal oxide prepared from the composite was layered externally on a metal surface. A fabricated steel plate was used to analyze its corrosion behavior in acidic solutions, namely, HCl, H_2SO4, and H3PO, acid solutions. The corrosion investigation of mild steel coated with epoxy-NiO, epoxy-CoO, and epoxy-$NiCo_2O_4$ nanocomposite was done using electrochemical techniques.

7.5.1 Weight loss measurement

Various corrosion parameters like surface coverage, inhibition efficiency and corrosion rate was determined by weight loss method and the values obtained were presented in **Table 7.10**. The WL (weight loss) of the mild steel was deliberately found by gradual increase of the inhibitor concentration (epoxy-NiO/epoxy-CoO/epoxy $NiCO_2O_4$) in 3M HCl, 1.5M H_2SO_4, and 0.5M H_3PO_4 and also in the absence of inhibitor. In this study the markable inhibition efficiency was shown in 3M HCl for all three inhibitors at higher concentration. The inhibitor gets adsorbed on the mild steel strongly which may due to the presence of heteroatoms. As the result of good surface coverage, it reduces the corrosion rate. The sequence of inhibitor efficacy was epoxy-NiO/epoxy-CoO/epoxy $NiCO_2O_4$, which confirms the anti-corrosive nature of the chosen material.

Table 7.10 *Corrosion parameter for various concentrations in mild steel by weight loss measurement at 303K*

Name of Inhibitor		Concentration (ppm)	Weight loss (g)	Corrosion rate (mmpy)	Surface coverage (θ)	%IE
Epoxy resin/ NiO	HCl	Blank	0.055	29.88		
		20	0.022	11.86	0.5981	59.81
		60	0.014	7.65	0.7407	74.07
		100	0.001	0.55	0.9815	98.15
	H_2SO_4	Blank	0.148	80.86		
		20	0.042	22.95	0.7162	71.62
		60	0.022	12.02	0.8429	84.29
		100	0.015	8.19	0.8929	89.29
	H_3PO_4	Blank	0.080	43.60		
		20	0.017	9.34	0.5807	58.07
		60	0.003	1.80	0.7085	70.85
		100	0.001	0.33	0.7335	73.35
Epoxy resin/ CoO	HCl	Blank	0.096	52.45		
		20	0.027	14.75	0.7188	71.88
		60	0.017	9.29	0.8229	82.29
		100	0.01	5.46	0.8958	89.58
	H_2SO_4	Blank	0.137	74.85		
		20	0.044	24.04	0.6788	67.88
		60	0.038	20.76	0.7226	72.26
		100	0.027	14.75	0.8029	80.29
	H_3PO_4	Blank	0.0986	53.87		
		20	0.0459	25.08	0.5345	53.45
		60	0.0307	16.77	0.5525	55.25
		100	0.0152	8.30	0.7784	77.84

Name of Inhibitor		Concentration (ppm)	Weight loss (g)	Corrosion rate (mmpy)	Surface coverage (θ)	%IE
Epoxy - $NiCo_2O_4$	HCl	Blank	0.23	125.65	-	-
		20	0.056	30.59	0.7565	75.65
		60	0.019	10.38	0.9174	91.74
		100	0.001	0.55	0.9957	99.57
	H_2SO_4	Blank	0.0871	47.58	-	-
		20	0.0282	15.41	0.6762	67.62
		60	0.0101	5.52	0.8840	88.40
		100	0.005	2.73	0.9426	94.26
	H_3PO_4	Blank	0.0686	37.48	-	-
		20	0.0152	8.30	0.7784	77.84
		60	0.0101	5.52	0.8528	85.28
		100	0.009	4.92	0.8688	86.88

7.5.2 Effect of temperature and activation parameters

Tables 7.11 and 7.12represent the weight loss measurements at higher temperature and values of ΔH˚, ΔS˚ & Ea. The %IE value is high at 303K with 100ppm inhibitor concentration. The inhibitor efficiency is in the order HCl > H_3PO_4> H_2SO_4. At higher temperature, adsorption between inhibitor and MS becomes weak and it creates a gap between film and steel. As a result, there will be a possibility of increased deterioration.

Figures 7.16 (a-i) and **7.17(a-i)** represent the Arrhenius and transition plots of log CR against 1/T for 20, 60 and 100 ppm of inhibitor concentrations. The uniformity in the results were found from the best fit of the plots. Therefore, it is easy to calculate the activation energy (Ea) from the slope of the straight line. Due to physical adsorption of the inhibitor on the surface of the mild steel (MS) the activation energy is high for epoxy-NiO/epoxy-CoO/epoxy $NiCO_2O_4$coated MS than compared with uncovered steel. The principle involved in this is, formation of compound between inhibitor and MS after coating, which in turn changes energy barrier thereby increases Ea. The presence of thin

metal oxide- epoxy resin does not permit the mass and energy(E) transfer. For H_2SO_4 & H_3PO_4, the activation energy is high at 100 ppm of inhibitor concentration and at lower concentration it shows fall in value which may be due to the formation of unstable film except epoxy-NiO, and epoxy-CoO inhibitor. But for 3M HCl, the highest Ea value is found at 100 ppm which proves the stability of film. For all three inhibitors, the highest activation energy was found only in HCl acid, which reveals the formation of stable compound with the film.

The enthalpy change (ΔH) shows positive value for all three acids and found to increase with increase in inhibitor concentration. But in general, there is no correlation between concentration and ΔH, but increase in concentration speeds up the formation of the film. It confirms that the energy barrier of the corrosion reaction with inhibitor was less, so the reactants crosses the barrier easily, the activated complex and products formed in the faster manner.

The ΔS of a chemical compound depends directly on molecular weight, nature of the molecule and also temperature. When the substance is divided into small parts, entropy will increase. In this case while applying the epoxy-NiO/epoxy-CoO/epoxy $NiCO_2O_4$ coating, the corrosion products become separated, as the result entropy increases. However, the change in entropy shows negative value only at lower concentration which evidences less disorderness and spontaneous reaction [5-6].

Table 7.11 Corrosion *parameters of mild steel solution in the presence and absence of epoxy-NiO/CoO/* $NiCO_2O_4$ *at different temperatures (303±K - 333±K)*

Inhibition concentration	Temp (K)	$NiCO_2O_4$			NiO			CoO		
		Weight loss (g)	Corrosion Rate (mmpy)	% IE	Weight loss (g)	Corrosion Rate (mmpy)	% IE	Weight loss (g)	Corrosion Rate (mmpy)	% IE
HCl	303	0.055	30.05		0.096	52.45		0.097	53.45	
	313	0.1497	81.78		0.099	54.09		0.001	55.09	
	323	0.2119	115.77		0.112	61.19		0.112	62.19	
	333	0.3221	175.97		0.121	66.11		0.121	67.11	
HCl +20ppm	303	0.022	12.02	60.00	0.027	14.75	71.88	0.027	15.75	72.87
	313	0.069	37.70	53.91	0.062	33.87	37.37	0.062	35.87	38.36
	323	0.137	74.85	35.35	0.089	48.62	20.54	0.089	49.62	21.53
	333	0.287	156.80	10.90	0.099	54.09	18.18	0.099	55.09	19.17
HCl +60ppm	303	0.014	7.65	74.55	0.017	9.29	82.29	0.017	10.29	83.28
	313	0.0545	29.77	63.59	0.041	22.40	58.59	0.041	23.40	57.58
	323	0.0925	50.54	56.35	0.068	37.15	39.29	0.068	38.15	38.27
	333	0.172	93.97	46.60	0.088	48.08	27.27	0.088	49.08	26.21
HCl +100ppm	303	0.001	0.55	98.18	0.01	5.46	89.58	0.01	6.46	87.59
	313	0.035	19.12	76.62	0.035	19.12	64.65	0.035	20.12	65.63
	323	0.089	48.62	58.00	0.089	48.62	20.54	0.089	49.62	21.51
	333	0.216	118.01	32.94	0.099	54.09	18.18	0.099	55.09	19.17
H_2SO_4	303	0.148	80.86		0.137	74.85		0.137	75.85	
	313	0.211	115.27		0.169	92.33		0.169	93.33	
	323	0.385	210.34		0.212	115.82		0.212	116.82	
	333	0.529	289.01		0.259	141.50		0.259	142.50	
H_2SO_4 + 20ppm	303	0.042	22.95	71.62	0.044	24.04	67.88	0.044	24.04	68.85
	313	0.073	39.88	65.40	0.068	37.15	59.76	0.068	38.15	57.73
	323	0.174	95.06	54.81	0.097	52.99	54.25	0.097	53.99	55.20
	333	0.298	162.80	43.67	0.142	77.58	45.17	0.142	78.58	46.19

Inhibition concentration	Temp (K)	$NiCO_2O_4$			NiO			CoO		
		Weight loss (g)	Corrosion Rate (mmpy)	% IE	Weight loss (g)	Corrosion Rate (mmpy)	% IE	Weight loss (g)	Corrosion Rate (mmpy)	% IE
H_2SO_4 + 60ppm	303	0.022	12.02	85.14	0.038	20.76	72.26	0.038	21.76	73.27
	313	0.079	43.16	62.56	0.065	35.51	61.54	0.065	36.51	62.55
	323	0.182	99.43	52.73	0.075	40.97	64.62	0.075	41.97	65.61
	333	0.271	148.05	48.77	0.142	77.58	45.17	0.142	78.58	46.19
H_2SO_4 + 100ppm	303	0.015	8.19	89.86	0.027	14.75	80.29	0.027	15.75	81.27
	313	0.0935	51.08	55.69	0.035	19.12	79.29	0.035	20.12	77.21
	323	0.1782	97.36	53.71	0.088	48.08	58.49	0.088	49.08	59.47
	333	0.36	196.68	31.95	0.157	85.77	39.38	0.157	86.77	38.35
H_3PO_4	303	0.08	43.71		0.0986	53.87		0.096	53.45	
	313	0.0972	53.10		0.1375	75.12		0.099	55.09	
	323	0.1199	65.50		0.1924	105.11		0.112	62.19	
	333	0.1387	75.78		0.2001	109.32		0.121	67.11	
H_3PO_4 + 20 ppm	303	0.017	9.29	78.75	0.0459	25.08	53.45	0.027	15.75	75.81
	313	0.031	16.94	68.11	0.025	13.66	81.82	0.062	34.87	38.36
	323	0.068	37.15	43.29	0.087	47.53	54.78	0.089	49.62	21.53
	333	0.093	50.81	32.95	0.132	72.11	34.03	0.099	55.09	19.17
H_3PO_4 + 60 ppm	303	0.003	1.64	96.25	0.0307	16.77	68.86	0.017	10.29	83.25
	313	0.045	24.58	53.70	0.06	32.78	56.36	0.041	23.40	57.57
	323	0.079	43.16	34.11	0.094	51.35	51.14	0.068	38.15	37.22
	333	0.099	54.09	28.62	0.148	80.86	26.04	0.088	49.08	29.22
H_3PO_4 + 100 ppm	303	0.001	0.55	98.75	0.0152	8.30	84.58	0.01	6.46	89.58
	313	0.0078	4.26	91.98	0.045	24.58	67.27	0.035	20.12	65.63
	323	0.0121	6.61	89.91	0.099	54.09	48.54	0.089	49.62	25.55
	333	0.0398	21.74	71.30	0.125	68.29	37.53	0.099	55.09	19.17

Table 7.12 *Activation parameters for the corrosion of mild steel*									
	NiO			**CoO**			**$NiCo_2O_4$**		
Inhibitor	**E_a (KJ)**	**ΔH° (KJ/mol)**	**E_a (KJ)**	**ΔH° (KJ/mol)**	**E_a (KJ)**	**ΔH° (KJ/mol)**	**ΔH° (KJ/mol)**	**E_a (KJ)**	**ΔH° (KJ/mol)**
HCl	47.69	45.05	47.69	45.05	47.69	45.05	39.19	36.55	24.86
HCl + 20ppm	82.3	67.94	82.3	67.94	82.3	67.94	17.28	14.64	104.82
HCl + 60ppm	67.93	59.04	67.93	59.04	67.93	59.04	94.83	92.19	138.78
HCl + 100ppm	144.4	141.8	144.4	141.8	144.4	141.8	105.04	62.23	14.95
H_2SO_4	37.10	34.46	37.10	34.46	37.10	34.46	46.15	43.51	11.40
H_2SO_4 + 20 ppm	56.58	53.94	56.58	53.94	56.58	53.94	70.86	68.22	60.40
H_2SO_4 + 60 ppm	70.63	67.99	70.63	67.99	70.63	67.99	104.45	101.81	164.09
H_2SO_4 + 100 ppm	85.96	83.32	85.96	83.32	85.96	83.32	113.57	85.04	155.84
H_3PO_4	15.63	12.99	15.63	12.99	15.63	12.99	61.78	59.14	39.99
H_3PO_4 + 20ppm	49.48	46.85	49.48	46.85	49.48	46.85	97.91	95.27	148.83
H_3PO_4 + 60ppm	94.00	91.36	94.00	91.36	94.00	91.36	108.05	105.41	178.36
H_3PO_4 + 100 ppm	96.82	94.18	96.82	94.18	96.82	94.18	179.95	62.30	209.64

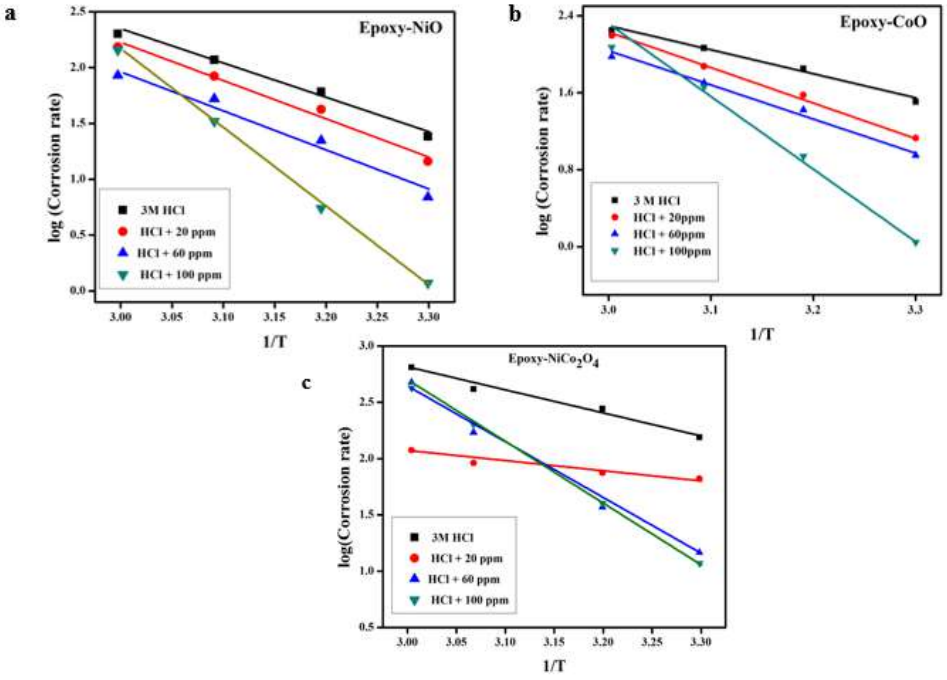

Figure 7.16 *Arrhenius plots of 3HCl a) epoxy-NiO b) epoxy-CoO c) epoxy- $NiCo_2O_4$*

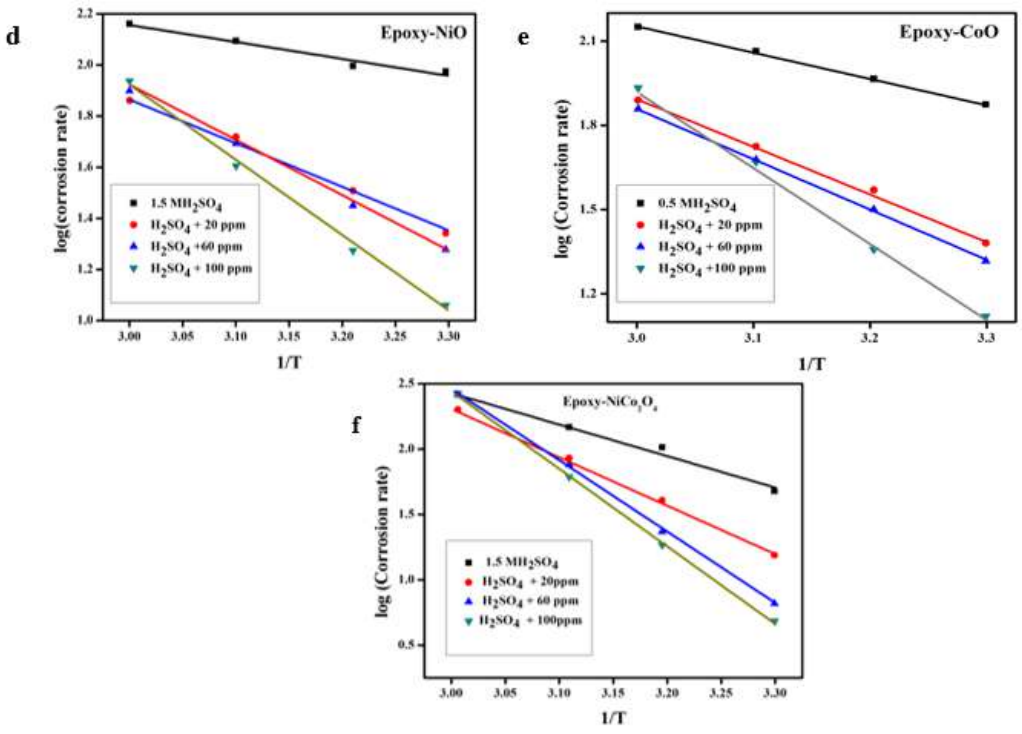

Figure 7.16 *Arrhenius plots of 1.5* H_2SO_4 *d) epoxy-NiO e) epoxy-CoO f) epoxy- $NiCo_2O_4$*

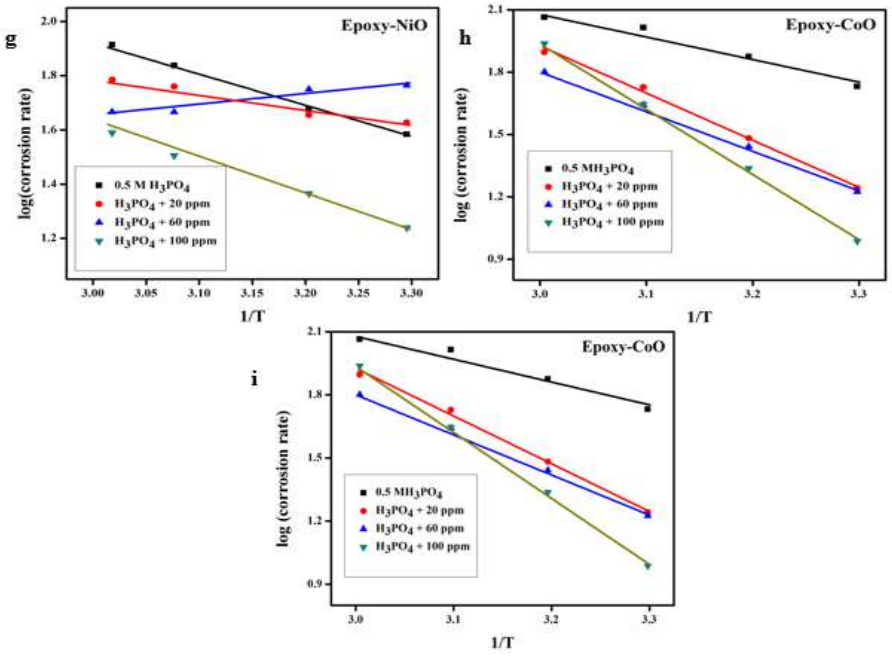

Figure 7.16 *Arrhenius plots of 0.5* H_3PO_4 *g) epoxy-NiO h) epoxy-CoO i) epoxy-* $NiCo_2O_4$

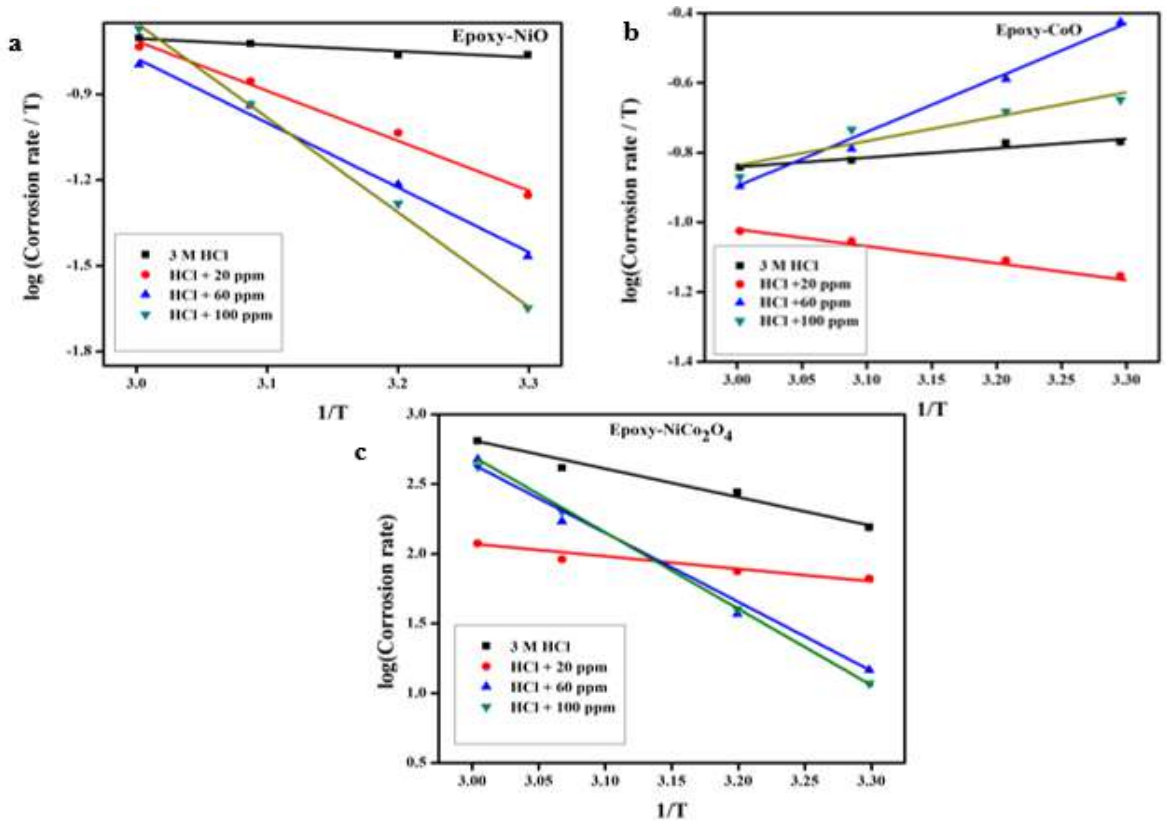

Figure 7.17 *Transition plots of 3HCl a) epoxy-NiO b) epoxy-CoO c) epoxy-* $NiCo_2O_4$

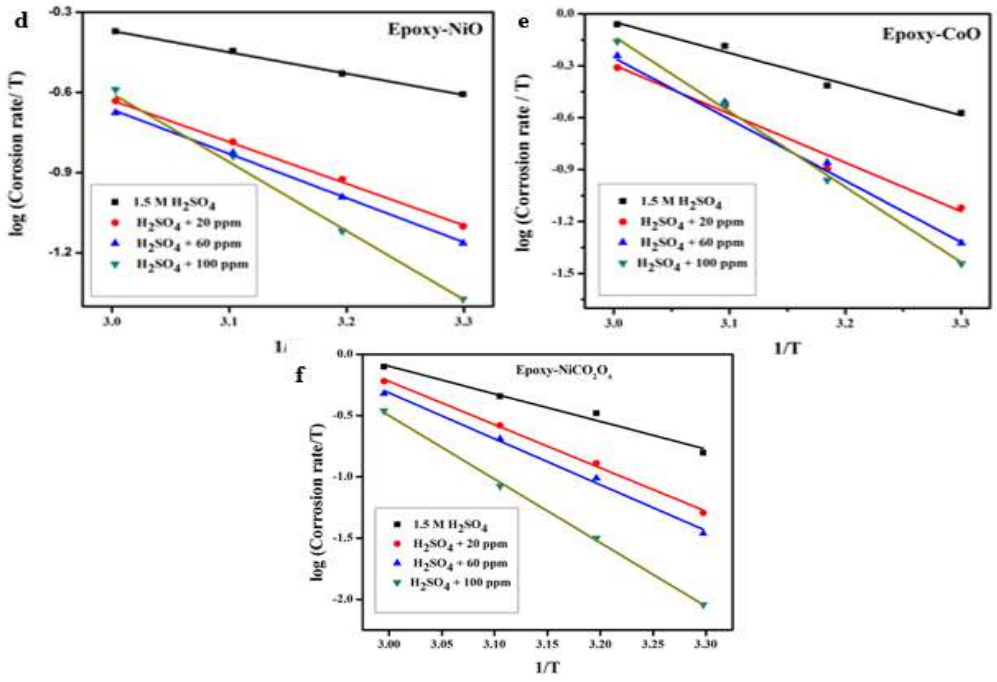

Figure 7.17 *Transition plots of 1.5* H_2SO_4 *d) epoxy-NiO e) epoxy-CoO f) epoxy-* $NiCo_2O_4$

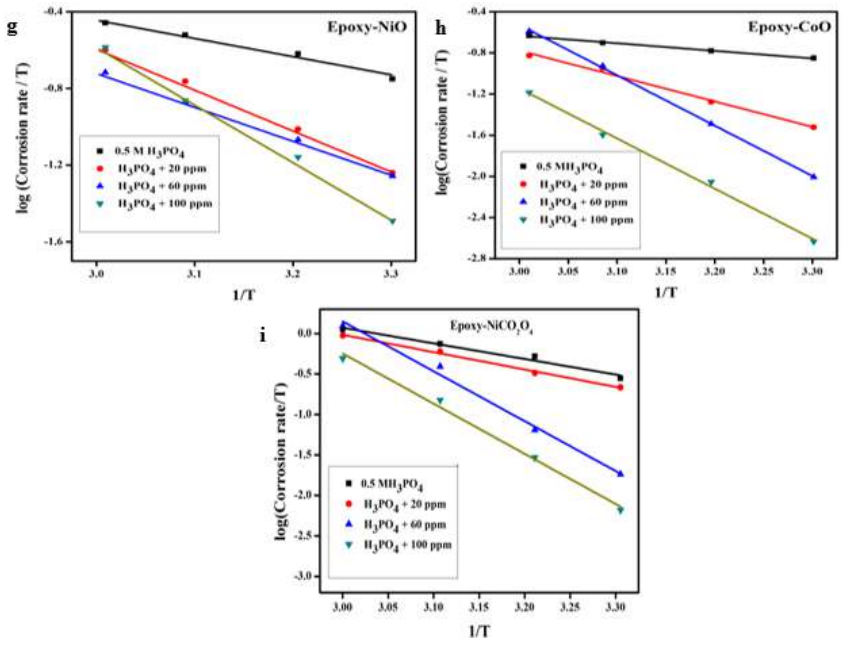

Figure 7.17 *Transition plots of 1.5* H_2SO_4 *g) epoxy-NiO eh) epoxy-CoO i) epoxy-* $NiCo_2O_4$

7.5.3 *Adsorption isotherms*

Adsorption isotherm provides some fundamental information about the interaction between epoxy-NiO/epoxy-CoO/ epoxy $NiCO_2O_4$ with MS. The value θ (fractional coverage value) concerning inhibitor concentration was obtained which is the necessary data to plot adsorption isotherm. Efforts were taken for the appropriate fit of θ value in different isotherms like Langmuir, Freundlich, and Frumkin which was shown in **Figure 7.18**. Inhibition of epoxy-NiO/epoxy-CoO/ epoxy $NiCO_2O_4$ to MS in 3M HCl, 1.5M H_2SO_4, and 0.5M H_3PO_4 obeys Langmuir isotherm. The correlation coefficient (R^2) was evaluated for all 3 inhibitors which is shown in **Table 7.13**. For all three acids, the linear best fit was attained by Langmuir isotherm with R2 values. From the correlation coefficient value, we can able to conclude the validity of the Langmuir approach and it shows good protection efficiency for epoxy-NiO/epoxy-CoO/ epoxy $NiCO_2O_4$.

In acidic media, anions in the acids are adsorbed quickly to the surface of the metal as a result the cationic and neutral particle adsorption will be limited due to excessive concentration of anions on the metal surface. Only because of this electrostatic interaction does the L/metal oxide inhibitor get adsorbed on the charged metal surface. Anions with a degree of hydration will be adsorbed stronger, and produce a -ve charge, so more cations will be adsorbed. But the phosphate and sulphate have lower adsorption than chloride ions which may be due to the lower interference property of these two ions[8].

The standard adsorption free energy was calculated below the equation which gives the relation between k and ΔG°_{ads}

$$\Delta G^{\circ}_{ads} = -RTLn(55.5K_{ads}) \qquad \textbf{Eq. (7.5)}$$

Where, ΔG°_{ads} is the standard adsorption-free energy, R – gas constant, T- temperature, 55.5 –concentration of water in the solution, and K_{ads} – Equilibrium constant of the adsorption process. The results are shown in **Table 7.14**.

The free energy shows a negative value for all the inhibitors in acidic media confirming the spontaneity and stability of the adsorption reaction. The ΔG°_{ads} values lie between the -20KJ/mol and -40KJ/mol, indicating both physisorption and chemisorption and complex type bond formation between inhibitor and MS.

Table 7.13 *The correlation coefficient (R^2) value obtained from adsorption isotherm with epoxy-L/NiO/CoO*					
Inhibitor		**Adsorption Isotherm**			
		Langmuir	**Freunlich**	**Frumkin**	**Temkin**
HCl	**epoxy -NiO**	0.999	0.871	0.871	0.861
	epoxy -CoO	0.995	0.996	0.996	0.994
	epoxy $NiCO_2O_4$	0.99	0.99	0.89	0.97
H_2SO_4	**epoxy -NiO**	0.994	0.871	0.871	0.861
	epoxy -CoO	0.994	0.976	0.976	0.985
	epoxy $NiCO_2O_4$	0.99	0.98	0.88	0.98
H_3PO_4	**epoxy -NiO**	0.994	0.871	0.871	0.861
	epoxy -CoO	0.999	0.984	0.984	0.989
	epoxy $NiCO_2O_4$	0.99	0.97	0.66	0.68

Table 7.14 Thermodynamic *parameters obtained for the epoxy-L/NiO/CoO/* epoxy $NiCO_2O_4$		
Inhibitor		**Langmuir**
		ΔG°_{ads} (kJ/mol)
HCl	**epoxy -NiO**	-25.50
	epoxy -CoO	-23.29
	Epoxy -$NiCo_2O_4$	-17.17
H_2SO_4	**epoxy -NiO**	-23.28
	epoxy -CoO	-22.87
	Epoxy -$NiCo_2O_4$	-18.35
H_3PO_4	**epoxy -NiO**	-23.91
	epoxy -CoO	-25.31
	Epoxy -$NiCo_2O_4$	-15.64

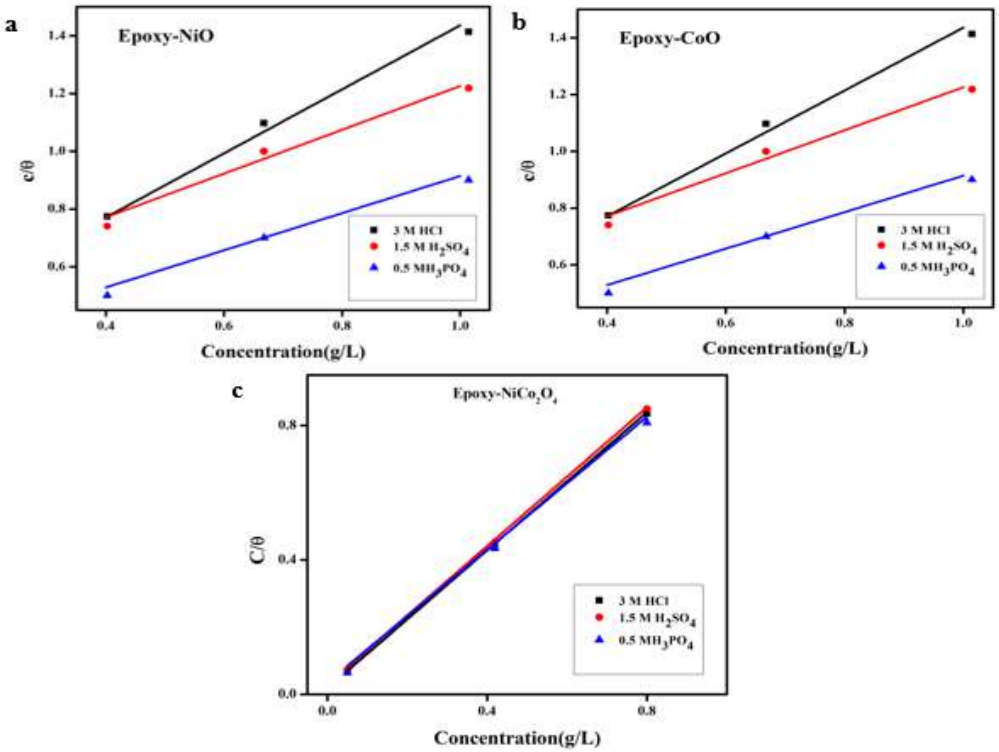

Figure 7.18 *Langmuir isotherm a) NiO, b) CoO, and c) $NiCo_2O_4$*

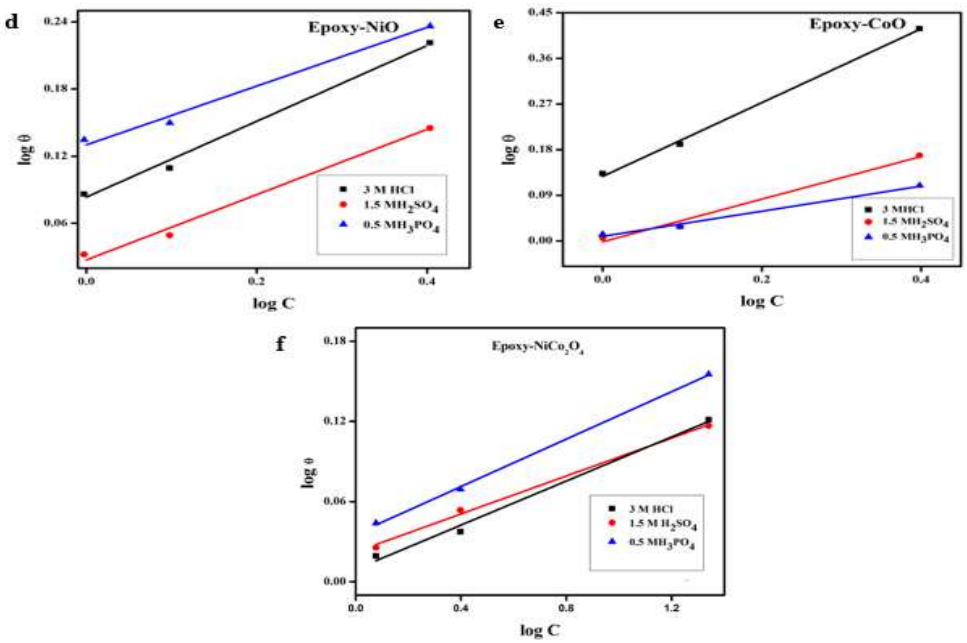

Figure 7.18 *Freundlich isotherm a) NiO, b) CoO, and c) $NiCo_2O_4$*

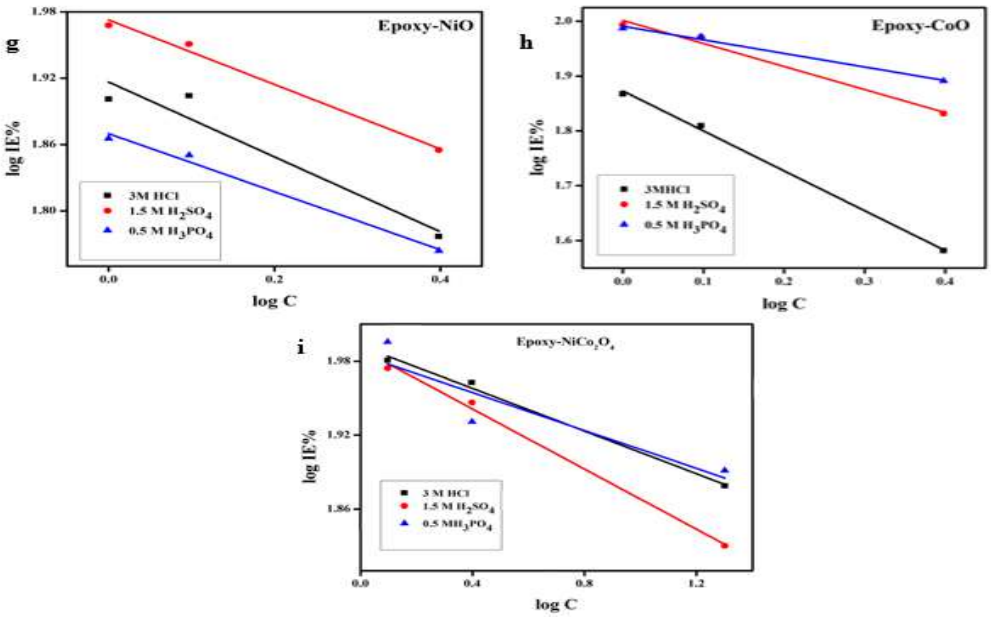

Figure 7.18 *Frumkin isotherm a) NiO, b) CoO, and c) $NiCo_2O_4$*

7.5.4 Electrochemical impedance spectroscopy

From EIS measurements, the protection properties of uncoated and epoxy-NiO/ epoxy-CoO/ epoxy $NiCO_2O_4$ coated on MS were determined in 3M HCl, 1.5M H_2SO_4, and 0.5M H_3PO_4. **Figure 7.19** shows a distinctive set of Nyquist plots for blank and different inhibitor concentrations and **Figure 7.20** shows an equivalent circuit for EIS measurement. From the plots, it is evident that the impedance response of MS in a blank solution of HCl, H_2SO_4, and H_3PO_4 has pointedly increased after the film. Mixing 20 ppm of epoxy-NiO/epoxy-CoO/ epoxy $NiCO_2O_4$ into epoxy resin reduces corrosion current compared to blank. With curiosity, we increased the inhibitor concentration from 20 ppm to 100 ppm. The results show the boosted protection efficiency of nanometal oxides.

From the Nyquist plot, the kinetic parameters for the corrosion process were determined and presented in **Table 7.15**. In EIS spectra exhibit a greater capacitive loop at the higher frequencies which were followed by the minor inductive loop at a low frequency. The capacitive loop shows that the corrosion of mild steel is mostly controlled by the charge transfer process. In HCl, H_2SO_4 and H_3PO_4 acid low frequency of the inductive loop may be attributed to forming reduction process obtained by adsorption occurred (Cl^-_{ads}, $SO_4^-{}_{ads}$, and $PO_4^-{}_{ads}$) and ($H^+{}_{ads}$) on the surface of the electrode which produces re-

dissolution produce at low frequencies to form passivated surface. The value of double layer capacitance (C_{dl}) was calculated by using the following equation and falls when the inhibitor concentration increases. [9-10]

$$C_{dl} = \frac{1}{2\pi f_{max}} * \frac{1}{R_{ct}} \quad \textbf{Eq. (7.6)}$$

The same results were obtained for all three inhibitors. The decreased value of C_{dl} is due to variation in the dielectric constant. which may be due to the formation of Fe-phosphate compared to the other two products and settling more effectively on the surface of the MS. In the H_3PO_4 medium the Nyquist plots are composed of two parts, slightly depressed capacitive loops occurred in the high-frequency region, and the inductive loop occurred in the lowered-frequency region. The high-frequency (capacitive loop) which ascribed as a charge transfer resistance (R_t). The inductive loop capacitive caused due to the adsorption intermediate of the compound which may be due to the formation of Fe-phosphate compared to the other two products and settling more effectively on the surface of the MS.

The increase in R_{ct} value shows the absence of localized corrosion and confirms the presence of a protective layer on MS. The R_{ct} value increases with an increase in inhibitor concentration which confirms the continuous film-forming process on the surface of MS. The formation of a thick film decreases the pore size and stops the free movement of the active compound to the surface and thereby increasing the inhibitor efficiency. The protection efficiency (%IE) depends on bonding (interfacial) between the epoxy film with MS surface. Other factors which affect this are nano–particle–steel surface interaction and nanoparticle-epoxy interaction. In the former case, due to the Van der Waals force, there is a chance for attraction/repulsion between two particles and causing deterioration. But in the presence of epoxy resin with nano metal oxide enhanced performance in protection efficiency was seen.

In EIS, the corresponding Nyquist plots obtained in 3M HCl, 1.5M H_2SO_4, and 0.5M H_3PO_4 in the presence of epoxy film and absence of film at various concentrations were studied in mild steel at room temperature (303K) for epoxy-NiO/epoxy-CoO/ epoxy $NiCO_2O_4$. From **Table 7.15**, values of various concentrations were studied from the inhibitor at the charge transfer resistance (R_{ct}), the double-layer capacitance (C_{dl}), and

protection efficiency (IE %) which provides evidence that the impedance plot provided an aggressive medium. When the concentration of the inhibitor increase, protection efficiency also increases, and the double-layer capacitance value decreases with an increase in concentration. The higher protection efficiency in HCl is due to greater adsorption of Cl^- ion. This indicated that the HCl produces a major role in the protection process when compared with H_2SO_4, and H_3PO_4.

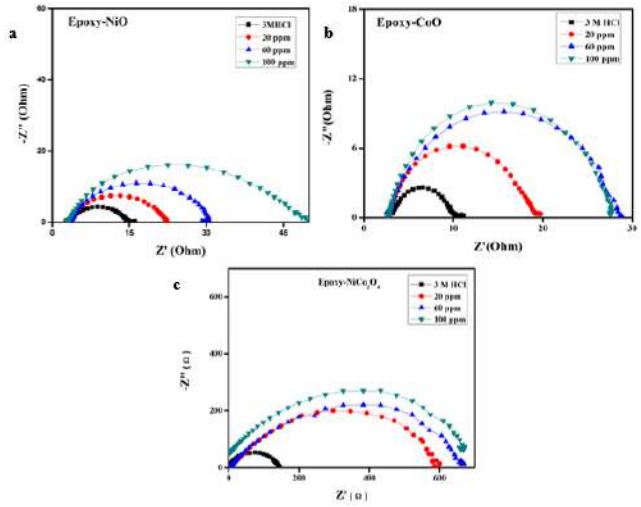

Figure 7.19 *Nyquist diagram for 3HCl a) epoxy-NiO b) epoxy-CoO c) epoxy- $NiCo_2O_4$*

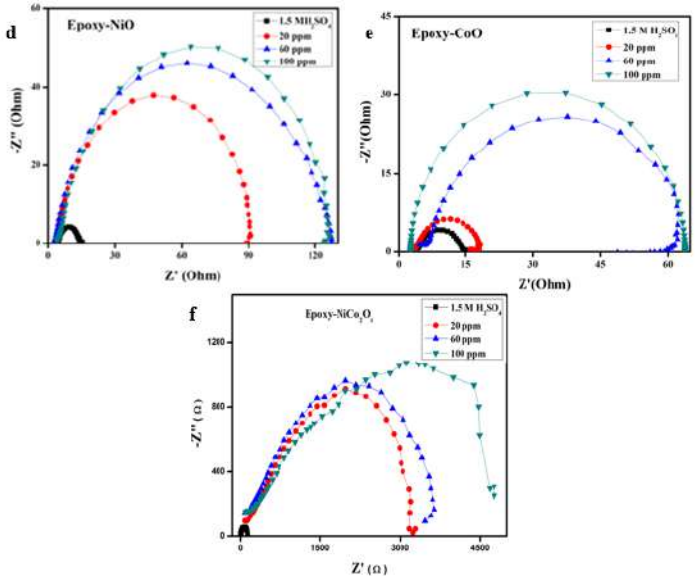

Figure 7.19 *Nyquist diagram for 1.5* H_2SO_4 *d) epoxy-NiO e) epoxy-CoO f) epoxy- $NiCo_2O_4$*

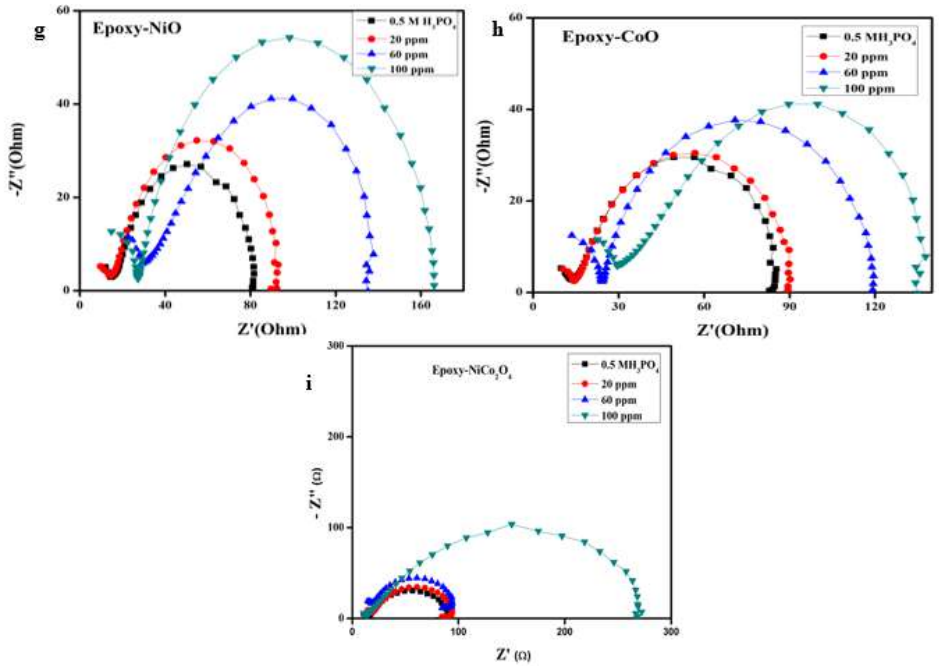

Figure 7.19 *Nyquist diagram for 0.5* H_3PO_4 *g) epoxy-NiO h) epoxy-CoO i) epoxy-* $NiCo_2O_4$

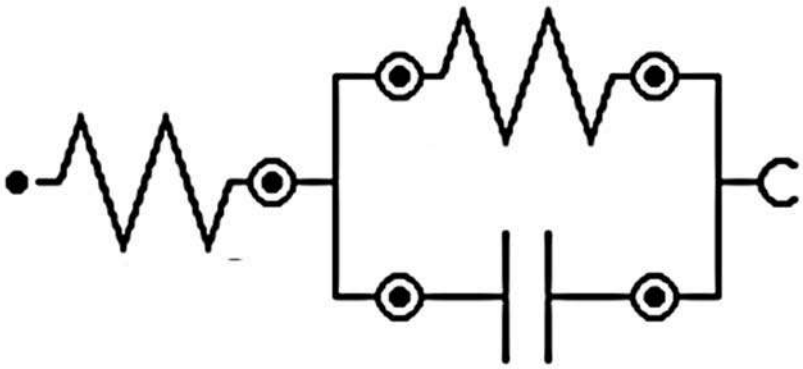

Figure 7.20 *Equivalent circuit model used*

***Table 7.15 Electrochemical** parameters at various concentrations*									
Inhibitor	**NiO**			**CoO**			**$NiCo_2O_4$**		
	R_{ct} (Ω m^2)	**C_{dl} ($\mu F/Cm^2$)**	**R_{ct} (Ω m^2)**	**C_{dl} ($\mu F/Cm^2$)**	**R_{ct} (Ω m^2)**	**C_{dl} ($\mu F/Cm^2$)**	**R_{ct} (Ω m^2)**	**C_{dl} ($\mu F/Cm^2$)**	**Inhibition Efficiency (%)**
HCl	3.34	18.5	3.34	18.5	3.34	18.5	7.26	24.9	
HCl + 20ppm	12.13	18.2	12.13	18.2	12.13	18.2	14.77	22.1	50.87
HCl + 60 ppm	20.46	17.8	20.46	17.8	20.46	17.8	21.77	18.5	66.65
HCl + 100 ppm	22.41	16.8	22.41	16.8	22.41	16.8	204.0	16.9	96.44
H_2SO_4	5.75	24.8	5.75	24.8	5.75	24.8	4.75	14.2	
H_2SO_4 + 20 ppm	9.37	19.9	9.37	19.9	9.37	19.9	79.02	12.7	93.98
H_2SO_4 + 60 ppm	16.17	15.4	16.17	15.4	16.17	15.4	108.3	9.7	95.61
H_2SO_4 + 100 ppm	35.17	13.2	35.17	13.2	35.17	13.2	114.6	7.7	95.85
H_3PO_4	1.01	43.2	1.01	43.22	1.01	43.22	45.15	29.3	
H_3PO_4 + 20 ppm	8.66	38.0	8.66	38.0	8.66	38.0	83.78	28.7	46.10
H_3PO_4 + 60ppm	20.98	24.1	20.98	24.1	20.98	24.1	166.5	26.2	72.88
H_3PO_4 + 100 ppm	21.73	22.2	21.73	22.2	21.73	22.2	545.9	24.1	91.73

7.5.5 *Potentiodynamic polarization*

The epoxy-NiO/epoxy-CoO/ epoxy $NiCO_2O_4$ coated steel substrate was exposed to polarization experiments which were carried out potentiometrically in view to know about the kinetics of cathodic and anodic reactions in acidic media. The resulting polarization curves were presented in **Figure 7.21** and the kinetic parameters obtained from the curves are tabulated in **Table 7.16**. There is the possibility of the inhibitor affects anodic (movement of M^{2+} from the electrode to solution phase) or cathodic (discharge of H^+ ions) or both. Since there is a change in both anodic and cathodic slope with a change in inhibitor

concentration, which means that the inhibitor affects both anode and cathode and behaves as a mixed-type inhibitor. Since there is a change in E_{corr} after the addition of the inhibitor it means that the energy effect is stronger in this particular inhibitor. When the I_{corr}, the corrosion current density decreases, E_{corr}, the corrosion potential move towards a negative value with an increase in inhibitor concentration. It confirms the good corrosion protection efficiency of epoxy-NiO/epoxy-CoO/ epoxy $NiCO_2O_4$. The E_{corr} value confirmed mixed type character [12]. This indicates that greater surface adsorption of epoxy- $NiCO_2O_4$ than other inhibitors.

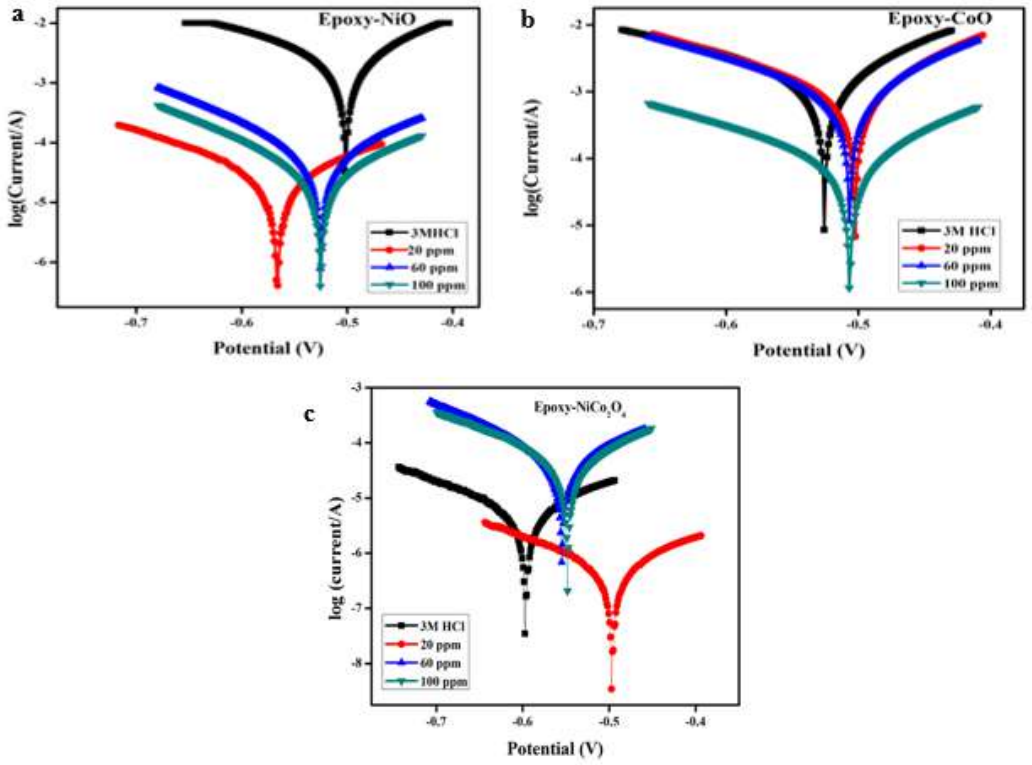

Figure 7.21 *Polarization diagram for 3HCl a) epoxy-NiO b) epoxy-CoO c) epoxy- $NiCo_2O_4$*

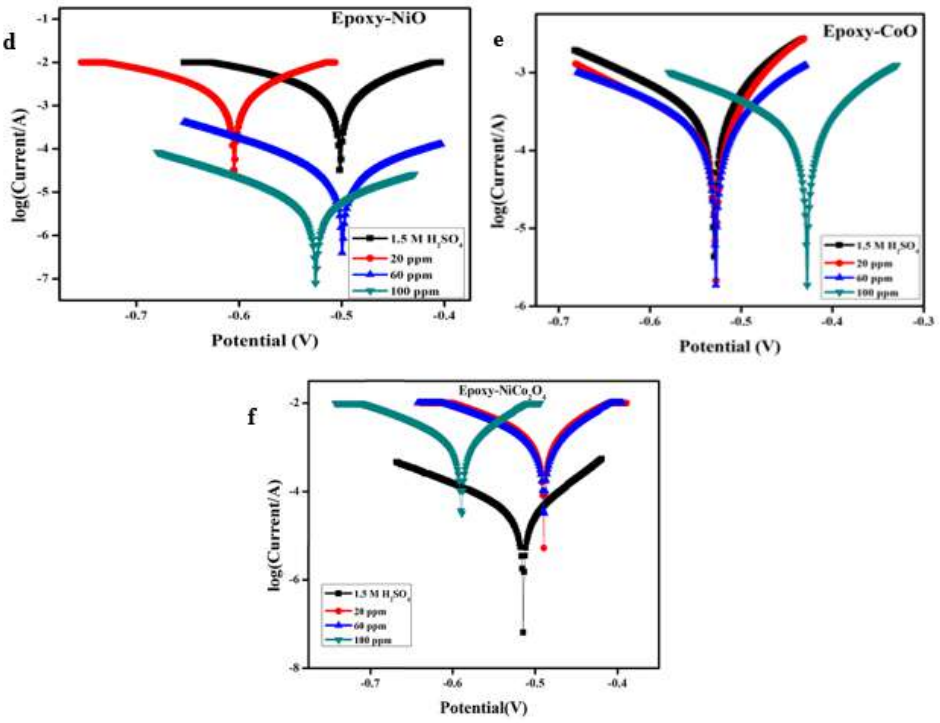

Figure 7.21 *Polarization diagram for 1.5* H_2SO_4 *d) epoxy-NiO e) epoxy-CoO f) epoxy-* $NiCo_2O_4$

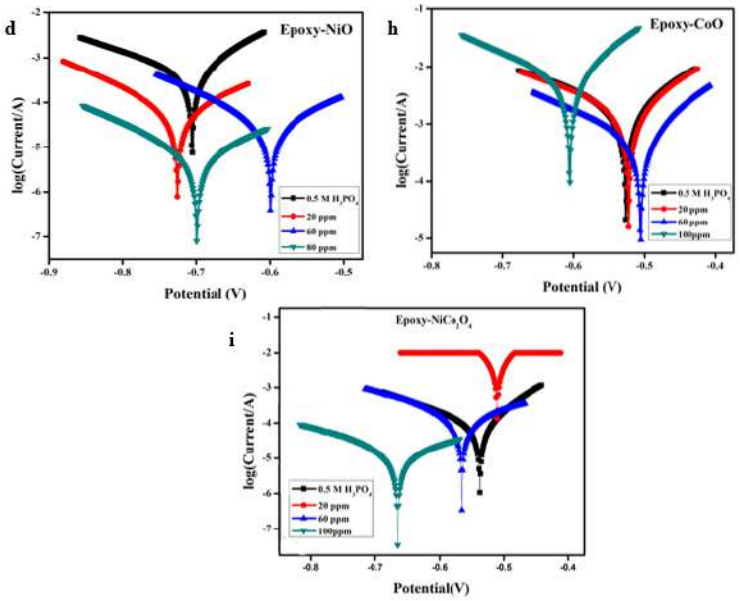

Figure 7.21 *Polarization diagram for 0.5* H_3PO_4 *g) epoxy-NiO h) epoxy-CoO i) epoxy-* $NiCo_2O_4$

Table 7.16 *Tafel polarization at various concentrations*

Inhibitor	NiO					CoO					$NiCo_2O_4$				
	Tafel slopes (mV/dec)		E_{corr} (mV)	I_{corr} ($\mu A/cm^2$)	IE (%)	Tafelslopes (mV/dec)		E_{corr} (mV)	I_{corr} ($\mu A/cm^2$)	IE (%)	Tafel slopes (mV/dec)		E_{corr} (mV)	I_{corr} ($\mu A/cm^2$)	IE (%)
	b_a	b_c				b_a	b_a				b_a	b_c			
HCl	215.7	119.2	-508	527		240	139	-525	413		315	132	-642	712	
HCl + 20 ppm	309.4	187.6	-501	219	58.44	209	124	-506	168	59.32	219	127	-539	857	60.8
HCl + 60 ppm	210.2	111.4	-500	121	77.03	198	108	-502	148	64.16	142	119	-512	522	80.2
HCl + 100 ppm	151.5	111.4	-485	102	80.64	179	101	-499	108	73.84	139	101	-403	119	90.8
H_2SO_4	231	128	-525	641		317.8	171.2	-525	724		298	122	-623	592	
H_2SO_4 + 20ppm	210	117.7	-505	211	67.08	133.5	60	-498	354	51.10	251	115	-521	397	56.8
H_2SO_4 + 60ppm	189	155.6	-522	152	69.72	116	53	-490	243	66.43	174	105	-422	254	79.2
H_2SO_4+100ppm	177	149	-485	132	73.70	108	48	-485	172	76.24	160	87	-402	111	82.7
H_3PO_4	325	153.3	-527	845		325	153.3	-527	845		435	169	-498	687	
H_3PO_4+20 ppm	277.7	94	-528	551	34.79	263.8	117.2	-529	569	32.66	357	138	-439	491	40.8
H_3PO_4+ 60ppm	312.5	119.1	-529	521	38.34	246.7	86	-527	426	49.58	258	118	-401	357	60.5
H_3PO_4+100 ppm	289.9	108.5	-489	316	62.60	231.8	78	-500	298	64.73	189	109	-312	216	75.1

7.5.6 *Micrograph SEM/TEM*

The SEM images of nano NiO and $NiCO_2O_4$ are shown in **Figure 7.22(a, b)** confirming that the nano metal oxide had a homogeneous shape and size but demonstrated slight agglomeration owing to the presence of legends, given that the nano metal oxide was dispersed in the powder form to perform the SEM analysis. The SEM analysis revealed a spherical structure, which supports the glassy nature of the nano metal oxide. Further, the energy dispersive X-ray (EDX) analysis **(Figure 7.22c)**, which shows the presence of three elements, ie., Ni, Co, and O, also confirms the nanostructure of $NiCo_2O_4$. Furthermore, the TEM and HR-TEM analysis **(Figure 7.22 d)** revealed the shape and average particle size. The obtained average particle size from the quantitative analysis performed from the TEM micrograph was 138.5 nm and the particles were spherical, which is consistent with the obtained SEM micrograph. Moreover, the HR-TEM image taken at 5 nm **(Figure 7.22 d)** reveals that the interference fringes with the d- spacing values of 0.33 nm and 0.28 nm correspond to the (220) and (311) planes of the $NiCo_2O_4$ crystal, respectively.

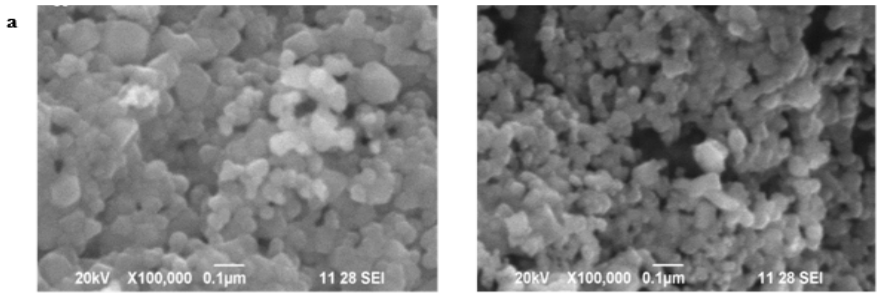

Figure 7.22 *SEM image of a) NiO*

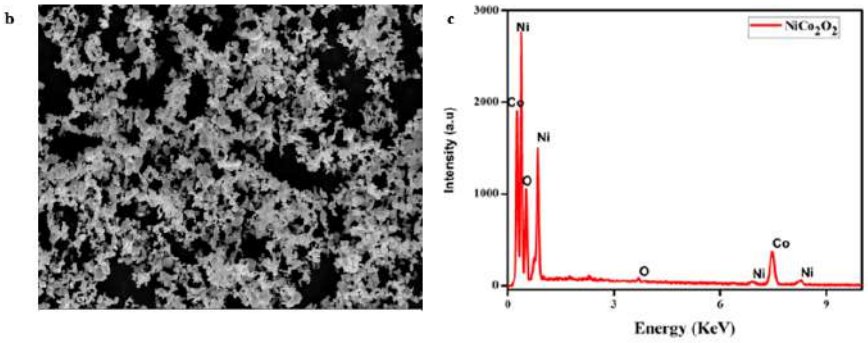

Figure 7.22 *SEM image of b) $NiCO_2O_4$ c) EDAX of $NiCO_2O_4$*

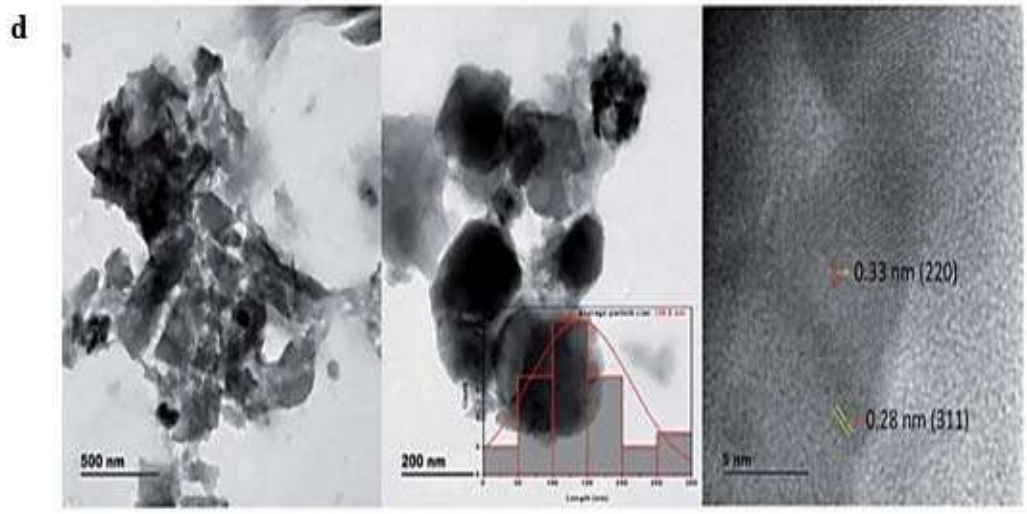

Figure 7.22 *TEM image of d) $NiCO_2O_4$*

7.5.7 *Scanning electron microscopy of mild steel*

SEM micrographs **(Figure 7.23)** reveal the changes that take place in the surface of the mild steel in the presence and absence of an inhibitor. The left side indicates the uncoated image shows a rough surface right side indicated the coated inhibitor image of HCl displays the smooth surface of MS in the absence of the inhibitor confirming the formation of a protective layer with inhibitor [13].

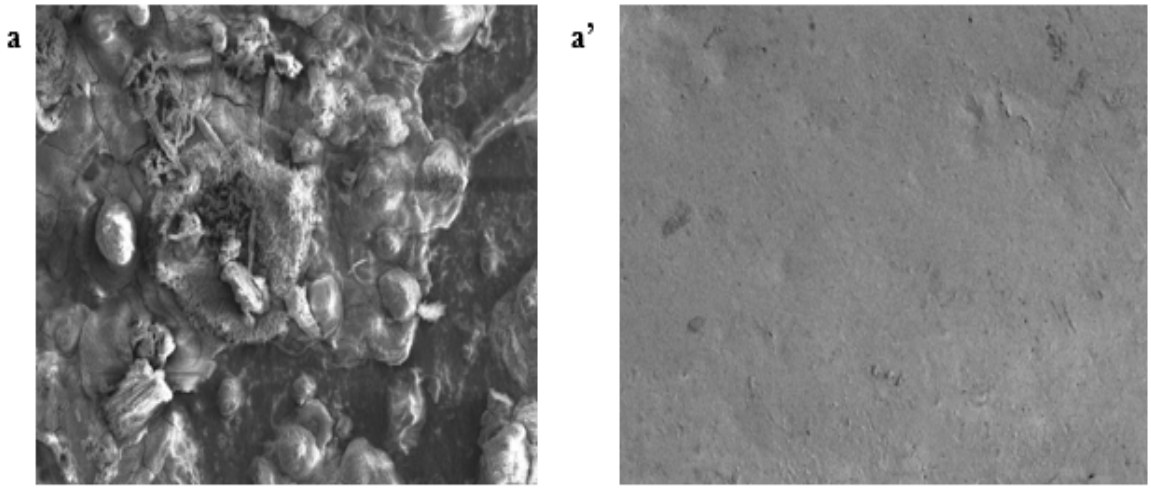

Figure 7.23 *SEM image of HCl in mild steel a) Absence of NiO a') Presence of NiO*

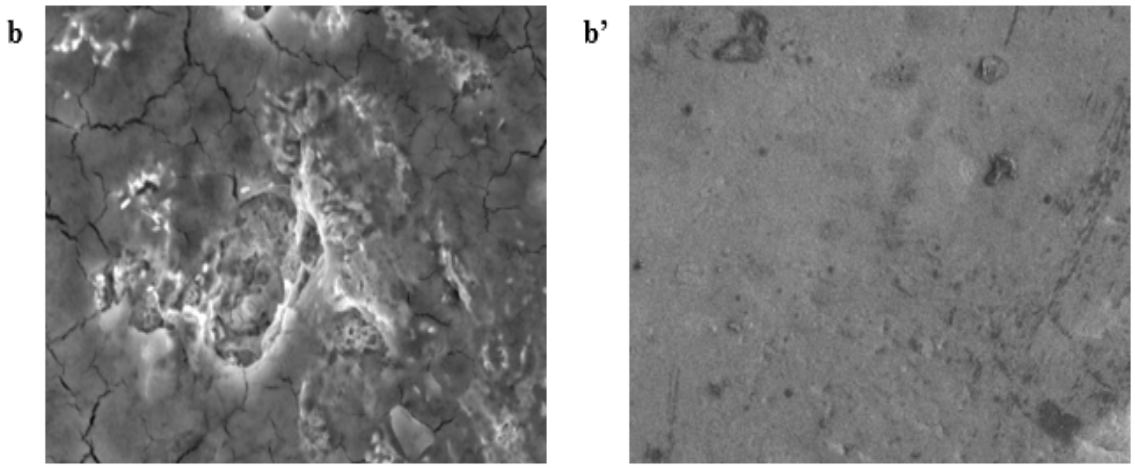

Figure 7.23 *SEM image of HCl in mild steel b) Absence of CoO b') Presence of CoO*

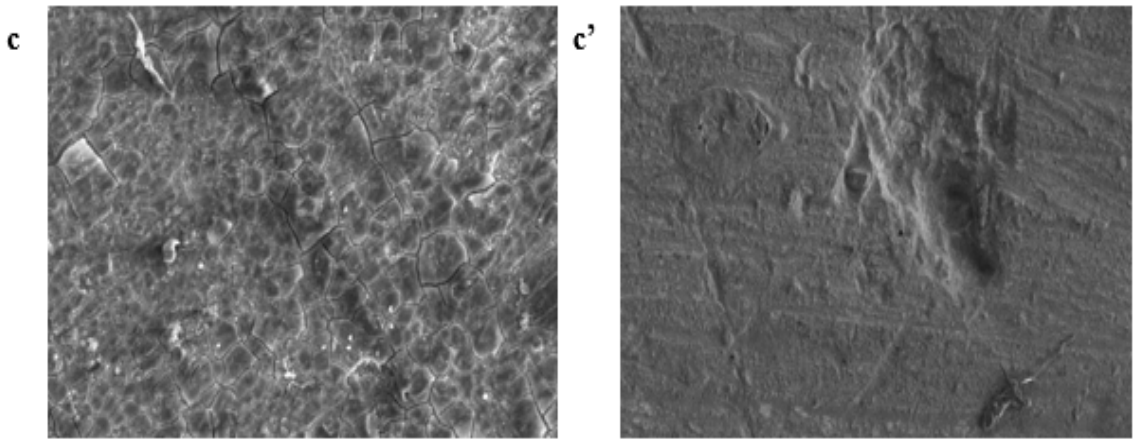

Figure 7.23 *SEM image of HCl in mild steel c) Absence of $NiCO_2O_4$*

c') Presence of $NiCO_2O_4$

7.5.8 *Proposed mechanism*

Donor-acceptor interactions of inhibitor molecules with mild steel are the key step of the corrosion mechanism **(Figure 7.24)**. The presence of nitrogen and oxygen atoms with unshared pairs of electrons will easily undergo protonation and exit as a cationic form in an acidic solution. For epoxy-Ni, epoxy-Co, and epoxy$NiCO_2O_4$ inhibitors oxidation

makes the steel surface positively charged which then attracts negative species from acids like Cl^{2-} SO_4^{2-} and PO_4^{2-} through electrostatic interactions.

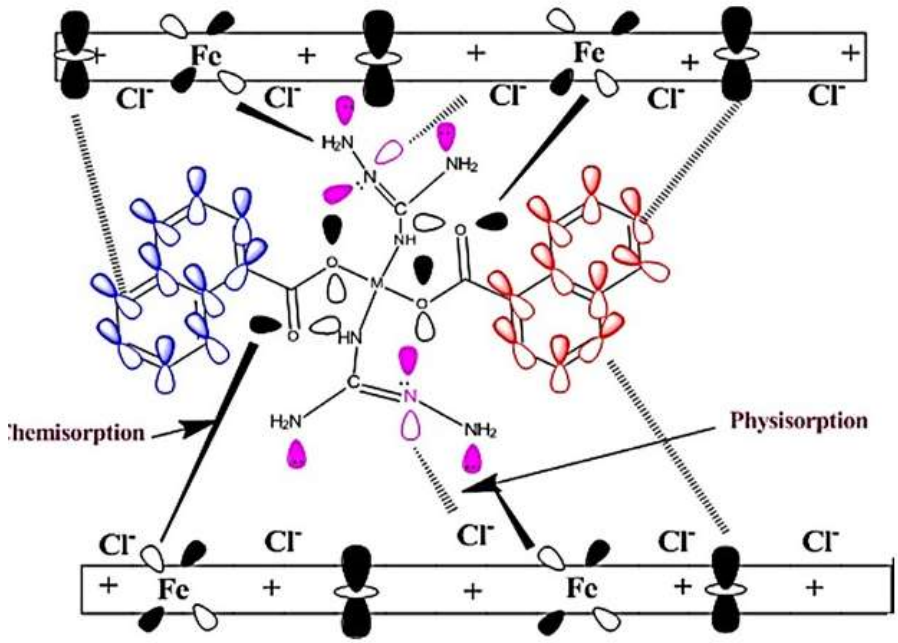

Figure 7.24 *Proposed mechanism*

7.6 CONCLUSION

In this work we discussed about the aminoguanidinium-1-naphthoate with metal ions like Mn^{2+}, Co^{2+}, Ni^{2+}, Cu^{2+}, Zn^{2+}, Cd^{2+}, Mg^{2+}, Ca^{2+}, Sr^{2+}, Ba^{2+}, Li^{+}, Na^{+}, and K^{+}. Systematic synthesis and characterization by analytical, spectral, thermal, and structural methods of complexes were carried out. FT-IR spectral study reveals the nature of the functional groups and vibrational modes of the metal complexes. In UV-visible spectra, the peak at 250-350 nm corresponds to $\pi \rightarrow \pi^*$ transition and the peak at 362-400 nm is due to the aminoguanidine group with band gap energy of 3.5-4.7 eV. TG-DTA result shows a majority of decomposition occurs around 230-395°C and confirms the stability of the metal complexes. Powder XRD indicates the isomorphism among the metal complexes. Zn (II) complex shows better antibacterial activity against Escherichia coli. Further complexes show good cytotoxic effects towards MCF-7(breast cancer) and A-549 (lung cancer).

The Application of the synthesized alkali and alkaline earth metals was compared and presented based on electrochemical studies. Linear sweep voltammetry (LSV) curves display excellent activity and the Tafel slope was found in the range of 6.38 to 40 $mVdec^{-1}$ in 0.5 M H_2SO_4. The electrochemical impedance spectroscopy (EIS) test was accomplished to recognize the mechanism of HER, and charge transfer resistance was less which indicates that composites are favorable for the hydrogen evolution. The electrochemical surface area (ECSA) was figured by studying the electric double-layer capacitance (C_{dl}) and it was found to be 0.377 μFcm^2 - 0.143 μFcm^2. More prominent ECSA values imply the target complexes have enhanced electrochemically active/dynamic sites and better hydrogen evolution performance. According to the results, high-performing catalytically active sites are found to be Li[1NA-AMG] metal ions. Furthermore, in a volcano plot, the position of the Li[1NA-AMG] metal ions is found to be close to the near thermoneutral catalytic activity. Based on the results, we successfully designed an electrocatalyst as a prospective candidate for hydrogen evolution reaction. In addition, nano oxide of ligand and Ni-Co composites were performed. Powder XRD diffraction was employed to characterize the ligand and metal composite, confirming the linkage of acid and base moiety with the metal ions. In the FT-IR analysis, the two different bands of M–O showed the linkage of the two metal ions in the composite.

Further, the decomposition of the metal composite resulted in the formation of $NiCo_2O_4$ as the end product. Epoxy-ligand/$NiCo_2O_4$ was examined for its anticorrosive property using mild steel in three different types of acids including HCl, H_2SO_4, and H_3PO_4 at different concentrations. Langmuir adsorption isotherm evidenced the excellent link between epoxy-$NiCo_2O_4$ and the exterior surface of the chosen mild steel specimen with a physisorption process. The Tafel plot result confirmed the mixed-mode corrosion protection behavior. The protection efficiency showed that epoxy-$NiCo_2O_4$ was a better inhibitor than epoxy-L in 3M hydrochloric acid. The anti-corrosion layer formed by the inhibitors had outstanding barrier potential by hindering the exchange of H_2O, O_2, and corrosive particles. The surface morphology of NiO, CoO, and $NiCo_2O_4$ was investigated using SEM (50nm) and TEM (138nm) and shows noteworthy anticorrosive properties. Thus, the synthesized mixed metal complex can be utilized in numerous industries for corrosion protection, which will be beneficial for achieving sustainability.

REFERENCES

1. Swathika, M. *et al.* Design and synergistic effect of nano-sized epoxy-NiCo2O4 nanocomposites for anticorrosion applications. *RSC Adv.* **12**, 14888–14901 (2022).
2. Arunadevi, N. *et al.* Structural, optical, thermal, biological and molecular docking studies of guanidine based naphthoate metal complexes. *Surfaces and Interfaces* **24**, 101094 (2021).
3. Hameed, A. S. H. *et al.* Impact of alkaline metal ions Mg2+, Ca2+, Sr2+ and Ba2+ on the structural, optical, thermal and antibacterial properties of ZnO nanoparticles prepared by the co-precipitation method. *J. Mater. Chem. B* **1**, 5950–5962 (2013).
4. Khadom, A. A. & Abdul-Hadi, A. A. Kinetic and mathematical approaches to the corrosion of mild steel in nitric acid. *React. Kinet. Mech. Catal. 2014 1121* **112**, 15–26 (2014).
5. Babić-Samardžija, K., Khaled, K. F. & Hackerman, N. N-heterocyclic amines and derivatives as corrosion inhibitors for iron in perchloric acid. *Anti-Corrosion Methods Mater.* **52**, 11–21 (2005).
6. Kadhim, A. *et al.* Experimental and theoretical studies of benzoxazines corrosion inhibitors. *Results Phys.* **7**, 4013–4019 (2017).
7. Xavier, J. R. Electrochemical, mechanical and adhesive properties of surface modified NiO-epoxy nanocomposite coatings on mild steel. *Mater. Sci. Eng. B* **260**, 114639 (2020).
8. Senhaji, O. *et al.* Experimental and Theoretical Study for Corrosion Inhibition in Normal Hydrochloric Acid Solution by Some New Phophonated Compounds. *Int. J. Electrochem. Sci* **6**, 6290–6299 (2011).
9. Saliyan, V. R. & Adhikari, A. V. Quinolin-5-ylmethylene-3-{[8-(trifluoromethyl)quinolin-4-yl]thio}propanohydrazide as an effective inhibitor of mild steel corrosion in HCl solution. *Corros. Sci.* **50**, 55–61 (2008).

10. Hashim, N. Z. N., Kahar, M. A. M., Kassim, K., Embong, Z. & Anouar, E. H. Experimental and theoretical studies of azomethines derived from benzylamine as corrosion inhibitors of mild steel in 1 M HCl. *J. Mol. Struct.* **1222**, 128899 (2020).

11. Zaidon, F. H. *et al.* Adsorption and corrosion inhibition accomplishment for thiosemicarbazone derivatives for mild steel in 1.0 M HCl medium: Electrochemical, XPS and DFT studies. *J. Mol. Liq.* **329**, 115553 (2021).

12. Amin, M. A. & Ibrahim, M. M. Corrosion and corrosion control of mild steel in concentrated H2SO4 solutions by a newly synthesized glycine derivative. *Corros. Sci.* **53**, 873–885 (2011).

13. Idouhli, R. *et al.* Electrochemical Studies of Monoterpenic Thiosemicarbazones as Corrosion Inhibitor for Steel in 1 M HCl. (2018) doi:10.1155/2018/9212705.